

# **Characterization of Surface and Interface Nanostructures by means of Specular and Diffuse X-ray Scattering**

vorgelegt von  
Diplom-Physiker  
Anton Haase  
geboren in Berlin

Von der Fakultät II - Mathematik und Naturwissenschaften  
der Technischen Universität Berlin  
zur Erlangung des akademischen Grades  
Doktor der Naturwissenschaften  
Dr. rer. nat.

genehmigte Dissertation

Promotionsausschuss:

Vorsitzender: Prof. Dr. Mister Unbekannt

Gutachter: Prof. Dr. Stefan Eisebitt

Gutachter: Prof. Dr. Mathias Richter

Gutachterin: Dr. Saša Bajt

Tag der wissenschaftlichen Aussprache:

Berlin 2017



# Abstract

English



# Zusammenfassung

Deutsch



# Contents

<b>1</b>	<b>Characterization of the Multilayer Structure for Different Systems</b>	<b>1</b>
1.1	Reconstruction Based on Specular EUV reflectance	2
1.1.1	Multilayer Model and Particle Swarm Optimization	3
1.1.2	The Problem of Model Uniqueness and Maximum Likelihood Estimation	7
1.2	Molybdenum Thickness Variation in Mo/Si/C Multilayers	11
1.2.1	Sample systems and experimental procedure	11
1.2.2	Combined Analysis of X-ray and EUV reflectance	14
1.2.3	Optimization results	18
1.3	Analysis of Cr/Sc Multilayers with Sub-nanometer Layer Thickness	20
1.3.1	Reconstruction with a discrete layer model approach	21
1.3.2	Extending The Model to Graded Interfaces and Interdiffusion	25
1.3.3	Addition of Complementary Experimental Methods	29
1.3.4	Reconstruction and Maximum Likelihood Evaluation	32
	<b>References</b>	<b>41</b>





# List of Figures

1.1	Spectrally resolved reflectance data of the Mo/B <sub>4</sub> C/Si/C multilayer sample. The irradiation was conducted under a fixed angle of incidence $\alpha_i = 15.0^\circ$ . The measurement uncertainty is within the line thickness of the plot. . . . .	2
1.2	Model of the multilayer stack including the substrate and the capping layers. The periodic part is enclosed between the dashed lines with four layers in each period repeated $N = 64$ times. The capping period does not include an interdiffusion layer but has a natural SiO <sub>2</sub> layer. . . . .	4
1.3	Theoretical reflectance curve based on the optimal model parameters obtained from the particle swarm optimization. . . . .	6
1.4	Parameter influence. . . . .	7
1.5	Results of the maximum likelihood estimation obtained via the Markov-chain Monte Carlo (MCMC) procedure. a) Two dimensional projection of the likelihood distribution for the parameter pair $d_{\text{Si}}$ and $d_{\text{Mo}}$ . The projection was obtained by marginalizing over all other parameters of the model. The black contours indicate the areas for one and two standard deviations (one and two sigma contours). The blue lines in all three sub-figures indicate the best parameter set found with the particle swarm optimization (PSO) method. b) One dimensional projection of the likelihood distribution for the silicon layer thickness $d_{\text{Si}}$ . The solid black line marks the center position (50% percentile) of the distribution. The dotted lines are the limits of one standard deviation. c) The one dimensional distribution similarly to b) for the molybdenum layer thickness. . . . .	9
1.6	In analogy to Fig. 1.5b and 1.5c the one dimensional projections of the likelihood distribution estimation for the Mo/B <sub>4</sub> C/Si/C sample are shown for the remaining parameters of the model with the PSO result, the center value and one standard deviation. . . . .	10
1.7	a) Reflectivity curves for the unpolished samples across the wavelength at a fixed angle of incidence of $\alpha_i = 15^\circ$ from the surface normal. The nine samples differ by the nominal Mo layer thickness indicated at the bottom axis. b) Reflectivity curves of the ten polished samples measured under the same conditions as for the first sample set. . . . .	12

## List of Figures

1.8	X-ray reflectivity (XRR) data for all unpolished and polished samples shown in dependence on the nominal molybdenum layer thickness $d_{\text{Mo}}^{\text{nom}}$ . In each of the subfigures a) and b) the XRR measurements for the sample with smallest and largest $d_{\text{Mo}}^{\text{nom}}$ are shown on the bottom and the top of the subfigure, respectively. In between, the XRR curves are illustrated in as a color map plot. . . . .	13
1.9	Model of the multilayer stack including the substrate and the capping layers. The periodic part is enclosed between the dashed lines with four layers in each period repeated 49 times. The capping period does not include an interdiffusion layer but has a natural $\text{SiO}_2$ layer and a carbon-like layer accounting for contamination on the top surface. . . . .	14
1.10	Combined analysis . . . . .	16
1.11	Two-dimensional likelihood distribution indicating the correlation of silicon and carbon layer thickness. The distribution was obtained by marginalizing over all remaining parameters of the model. The blue lines indicate the fit obtained through the two-step MCMC optimization procedure (see main text). . . . .	17
1.12	Experimental data in comparison with the theoretical curves calculated with the model parameters obtained from the combined analysis of extreme ultraviolet (EUV) and XRR data. The data shown here was measured on the unpolished sample with nominal molybdenum thickness of $d_{\text{Mo}}^{\text{nom}} = 3.05 \text{ nm}$ .18	
1.13	a) Fitted Mo thickness values for both sample sets resulting from the MCMC analysis (see text). The nominal Mo layer thickness is shown in comparison in good agreement with the obtained thicknesses. b) Fitted total period thickness $D$ for both sample sets. For both sample sets, clear jumps can be observed at approx. $d_{\text{Mo}}^{\text{nom}} = 2.00 \text{ nm}$ and $d_{\text{Mo}}^{\text{nom}} = 2.38 \text{ nm}$ , respectively, which is attributed to the crystallization threshold (see text). The marked (circle) samples were measured and analyzed with respect to the diffuse scattering. . . . .	19
1.14	Peak reflectance values for each sample obtained from the EUV measurements for the unpolished sample set (a) and the polished sample set (b). The maximum theoretical reflectance is shown in both subfigures for a perfect (no roughness or interdiffusion) layer system with the same specifications as the samples. . . . .	20
1.15	Model of the multilayer stack including the substrate and the capping layers. The periodic part is enclosed between the dashed lines with four layers in each period repeated $N = 64$ times. The capping period does not include an interdiffusion layer but has a natural $\text{SiO}_2$ layer. . . . .	21
1.16	EUV and XRR . . . . .	22
1.17	Fitted experimental EUV reflectance curves across the wavelength of the radiation impinging at $\alpha_i = 1.5^\circ$ from normal, based on the binary model. The green curve shows the maximum possible reflectance assuming a perfect multilayer system without roughness or interdiffusion. . . . .	24

1.18	a) Measured EUV reflectivity curve for and near-normal angle of incidence of $\alpha_i = 1.5^\circ$ together with calculated curve of the PSO-based binary model reconstruction. b) Measured and calculated XRR curves for the same sample and model parameters at grazing angles of incidence using radiation at the $\text{Cu-K}_\alpha$ wavelength. A clear mismatch of the theoretical curve and the measured data can be observed for the second Bragg peak between $\alpha_i^{\text{GI}} = 5.0^\circ$ and $\alpha_i^{\text{GI}} = 6.0^\circ$ . . . . .	24
1.19	Binary and gradual Cr/Sc multilayer models. . . . .	26
1.20	Numerical uncertainty . . . . .	27
1.21	Comparison of the reconstructions of both models for the EUV and XRR data. a) Measured EUV reflectivity curve for and near-normal angle of incidence of $\alpha_i = 1.5^\circ$ together with calculated curve of the PSO-based binary model reconstruction. b) Measured and calculated XRR curves for the same sample and model parameters at grazing angles of incidence using radiation at the $\text{Cu-K}_\alpha$ wavelength. A clear mismatch of the theoretical curve and the measured data can be observed for the second Bragg peak between $\alpha_i^{\text{GI}} = 5.0^\circ$ and $\alpha_i^{\text{GI}} = 6.0^\circ$ . c) Measured EUV reflectivity curve for and near-normal angle of incidence of $\alpha_i = 1.5^\circ$ together with calculated curve of the PSO-based gradual model reconstruction. d) Measured and calculated XRR curves for the same sample and model parameters at grazing angles of incidence using radiation at the $\text{Cu-K}_\alpha$ wavelength. . .	28
1.22	REUV . . . . .	30
1.23	XRF . . . . .	31
1.24	All relevant data . . . . .	32
1.25	Measured and calculated reflectance and intensity curves for the optimized parameters with the combined analysis of all experiments as listed in Table ??	34
1.26	Cornerplot . . . . .	36
1.27	CrSc eta rho correlation . . . . .	37
1.28	Visual representation of the total confidence intervals for each of the parameters with respect to each of the individual experiments as well as the combined analysis. . . . .	38
1.29	Real part of the index of refraction $n$ based on the results of the optimized parameters listed in Table ?? for the combined analysis for a selected wavelength. The gradual interface model is shown in direct comparison to the binary model optimized for the EUV reflectance curve over three full periods. The resulting strong asymmetry in the width of the interface regions is clearly visible (see text). The gray and white shaded areas indicate the Cr and Sc layers, respectively, for the binary model. . . . .	39



# List of Tables

1.1	Multilayer parametrization and parameter limits . . . . .	4
1.2	Results for the ptimized parameters based on the PSO of the EUV reflectivity for the Mo/B <sub>4</sub> C/Si/C sample. . . . .	6
1.3	MCMC results obtained by the analysis of the EUV reflectivity for the Mo/B <sub>4</sub> C/Si/C sample. The center values (50% percentile) together with confidence intervals (c.i.) of one and two standard deviations are shown. . . . .	10
1.4	List of nominal molybdenum layer thicknesses in the two sample sets. Both sets were fabricated with a equidistant increase in thickness from 1.70 nm to 3.05 nm with 9 unpolished and 10 polished samples. . . . .	11
1.5	Parametrization of the Mo/Si/C multilayer samples with varying molybdenum layer thicknesses. . . . .	15
1.6	List of nominal molybdenum layer thicknesses in the two sample sets. Both sets were fabricated with a equidistant increase in thickness from 1.70 nm to 3.05 nm with 9 unpolished and 10 polished samples. . . . .	18
1.7	Parametrization of the Cr/Sc binary multilayer model. . . . .	22
1.8	PSO fit results for the discrete layer Cr/Sc multilayer model. The bulk multilayer parameters were obtained by exclusively applying the PSO method to the EUV data. The capping layer parameters were deducted from the XRR data excluding the Bragg peaks in a combined analysis. . .	23
1.9	Multilayer parametrization and parameter limits . . . . .	27
1.10	Optimized model parameters obtained by PSO analysis . . . . .	33
1.11	Optimized model parameters with confidence intervals derived from MCMC validation for each individual experiment and the combined analysis	34



# 1

## Characterization of the Multilayer Structure for Different Systems

The multilayer mirror samples we shall investigate here were fabricated using the magnetron sputtering technique briefly discussed in the chapter ?? with nominal layer thicknesses and chemical species, depending on the desired reflection angle and spectral range. Among other parameters of the production process, the achieved layer thickness and sharpness of the interfaces has a direct impact on the performance of these mirrors with respect to their peak reflectance and bandwidth. Although the sputtering process is a well established technique for mirror fabrication, the actual layer thicknesses in the sample may differ from the nominal values and are generally unknown.

Based on the matrix algorithm introduced in chapter ??, the electromagnetic fields inside and outside an arbitrary layer system can be calculated. Most importantly, this allows to calculate the expected specular reflectance curves across angular or spectral ranges for a given layer model. The comparison of these calculated curves to measured data thus allows to obtain information about the actual layer properties in a given sample. However, the detected reflectance values in a specular reflection experiment are merely intensities of reflected radiation. The information on the phase of the electromagnetic wave can not be obtained in this way and is lost. It is thus not possible to directly reconstruct the layout of the sample with the measured reflection curve. This is known as the inverse problem of scatterometry. Reconstructing the layer properties is therefore an attempt of solving this inverse problem by accumulating prior knowledge about the sample, such as the nominal design goals during the fabrication process, into a model of that system. Starting from this model, the theoretically calculated curve is compared to the measured reflectance and optimized iteratively.

This method is not limited to the optimization of the model with respect to the reflectance of the mirror samples in their designated EUV spectral range. In order to add complementary information for refining the solution of the inverse problem, additional methods can be applied. In this chapter, depending on the sample system, we analyze several experimental methods. Apart from the aforementioned reflectance in the EUV spectral range, we apply resonant EUV reflectance across absorption edges, XRR with

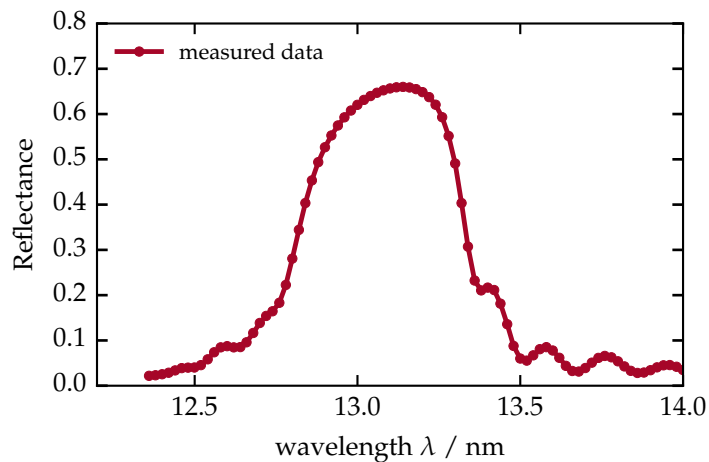
high photon energy and finally X-ray fluorescence (XRF). The latter does rely on the measurement of fluorescence radiation and thus requires the calculation of the field intensities inside the layer stack at the position of a specific chemical species for its analysis as described in section ?? of chapter ??.

## 1.1 Reconstruction Based on Specular EUV reflectance

In this section we demonstrate the reconstruction of a multilayer system designed as near-normal incidence mirror for the wavelength range between 12.4 nm and 14.0 nm based solely on experimental data of EUV reflectivity. The mirror was designed to achieve a peak in the reflectance at a wavelength of  $\lambda = 13.5$  nm for an angle of incidence of  $\alpha_i = 6^\circ$ . That combination is of relevance for optical setups in the next generation lithography setups for the semiconductor industry, for which this sample served as a prototype. The multilayer coating was deposited on a polished silicon substrate. The sample contains a periodic layer stack of molybdenum (Mo) and silicon (Si). Due to the problem of intermixing and resulting loss of interface definition, additional barrier layers of boroncarbide ( $B_4C$ ) and carbon (C) were included at the Mo to Si and Si to Mo interfaces, respectively. We shall therefore refer to this sample with the layer sequence within one period from bottom to top as Mo/ $B_4C$ /Si/C. The periodicity of that system is  $N = 65$ , while the 65th (capping) layer period does not possess a carbon layer but terminates with the silicon layer. A detailed schematic figure of the layer layout can be found in the description of the corresponding theoretical model in Fig. 1.2 below.

The sample was measured with respect to its reflectivity across the spectral range mentioned above at an angle of incidence of  $\alpha_i = 15^\circ$  from the surface normal. The measurement was conducted at the extreme ultraviolet beamline (EUVR) beamline at the metrology light source (MLS). The reflectivity was evaluated by first measuring the direct beam in the reflectometer with the diode detector. Then, the reflected radiation at an detector angle of  $30^\circ$  was measured in reference to the direct beam signal. To ensure the stability of the result, the direct beam was measured again afterwards and compared to the data of the first measurement. The normalized results are shown in Fig. 1.1. The measurement uncertainty in with this experimental method is within 1 % of the peak reflectance value. Consequently, the error margin is within the line thickness of the data presentation in Fig. 1.1.

**Figure 1.1** | Spectrally resolved reflectance data of the Mo/ $B_4C$ /Si/C multilayer sample. The irradiation was conducted under a fixed angle of incidence  $\alpha_i = 15.0^\circ$ . The measurement uncertainty is within the line thickness of the plot.



The reflectivity curve shows a broad peak attaining its maximum value at a wavelength



of approximately 13.1 nm, which is lower than the design peak reflectance of 13.5 nm. That is due to the different angle of incidence used in the experiment. Apart from the main peak, side fringes are visible. They originate due to a superposition of waves being reflected at the top surface and the substrate interface. They are thus directly related to the total thickness of the multilayer coating and well known as *Kiessig fringes* [20]. Based on the data obtained through this spectrally resolved reflectivity experiment, we shall attempt to reconstruct the unknown layer layout in the following sections. The nominal fabrication parameters serve as an anchor point for the analysis to construct a reasonable model for the reconstruction.

The reconstruction of a given model based on the evaluation of EUV (or XRR) reflectivity data is a well established method for the characterization of multilayer systems widely used today [3, 6, 23]. In most cases a model is constructed and optimized applying gradient methods such as the Levenberg-Marquardt method [22, 24]. Those optimization algorithms typically operate with a set of start parameters within the parameter space and iteratively improve the overlap of the prediction from the theoretical calculation and the experimental data. This is done by calculating the gradient of a minimization functional, usually termed  $\chi^2$ , in all directions in the parameter space and changing the parameters accordingly in direction of smaller  $\chi^2$  values. This approach has the major disadvantage that the end result is strongly dependent on the choice of starting values and may not represent a global minimum of  $\chi^2$  but only a local optimum. While estimations of the quality of the fit results within the (local) optimum are possible, no estimation can be given globally for the given model. For those reasons, this characterization strategy has only limited applicability and alternative approaches are required.

In contrast to those gradient methods, statistical optimization algorithms exist. They share the aim of minimizing a optimization functional  $\chi^2$  with the gradient approaches, but operate on the whole parameter space with predefined limits instead. In the following we shall apply those statistical optimization routines to obtain the reconstruction of the Mo/B<sub>4</sub>C/Si/C sample and elaborate their application to the characterization of multilayer systems in detail.

### 1.1.1 Multilayer Model and Particle Swarm Optimization

For the purpose of reconstructing the layer layout of the Mo/B<sub>4</sub>C/Si/C sample, a parameterized model is needed entering the theoretical calculations to obtain the reflectivity curve according to the matrix algorithm. The model is largely based on prior knowledge available from the fabrication process. For the multilayer sample investigated here, the nominal layer design is known and a schematic representation is shown in Fig. 1.2. As introduced above, the multilayer coating consists of a periodic arrangement of four layers replicated 64 times. With the top period being different from the others through the missing carbon interdiffusion layer on the top surface. Since the sample was exposed to ambient conditions, a passivation of the top silicon surface through oxidation has to be taken into account through a silicondioxide layer. The parameterization of that model is given by the thicknesses of each layer within one period as well as for the capping silicondioxide layer. Each of the deposited layers may vary in density with respect to the bulk density of that material [6], which also needs to be reflected in the model. Finally, the Nevot-Croce factor  $\sigma$  accounting for roughness and interdiffusion at the interfaces as introduced in chapter ?? is also included. The required optical constants, i.e. the indices of refraction, of the respective materials in the relevant spectral range are

## CHARACTERIZATION OF THE MULTILAYER STRUCTURE FOR DIFFERENT SYSTEMS

**Figure 1.2** | Model of the multilayer stack including the substrate and the capping layers. The periodic part is enclosed between the dashed lines with four layers in each period repeated  $N = 64$  times. The capping period does not include an interdiffusion layer but has a natural  $\text{SiO}_2$  layer.

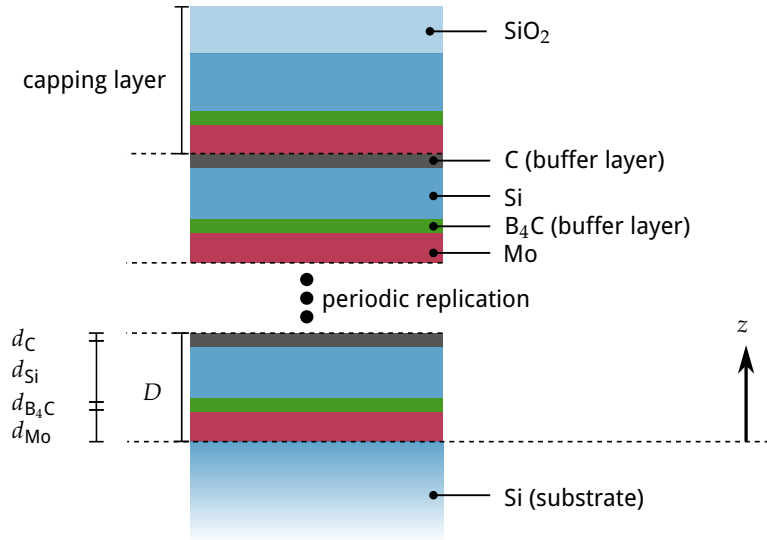


**Table 1.1** | Multilayer parametrization and parameter limits

Parameter	Definition	Lower bound	Upper bound
$d_{\text{Mo}}$ / nm	Mo layer thickness	0.0	7.0
$d_{\text{Si}}$ / nm	Si layer thickness	0.0	7.0
$d_{\text{C}}$ / nm	C buffer layer thickness	0.0	5.0
$d_{\text{B}_4\text{C}}$ / nm	$\text{B}_4\text{C}$ buffer layer thickness	0.0	5.0
$\sigma$ / nm	Nénot-Croce parameter (identical for all interfaces)	0.0	2.0
$\rho_{\text{Mo}}$	Mo density w.r.t. bulk density	0.5	1.0
$\rho_{\text{Si}}$	Si density w.r.t. bulk density	0.5	1.0
$\rho_{\text{C}}$	C density w.r.t. bulk density	0.5	1.0
$\rho_{\text{B}_4\text{C}}$	$\text{B}_4\text{C}$ density w.r.t. bulk density	0.5	1.0
Capping layer			
$d_{\text{SiO}_2(\text{cap})}$ / nm	$\text{SiO}_2$ capping layer thickness	0.0	5.0
$\rho_{\text{SiO}_2(\text{cap})}$	$= \rho_{\text{Si}}$ (identical to Si density)		

taken from tabulated values by Henke et al. [17] and used for the theoretical calculations based on the matrix algorithm. A full list of the model parameters for the multilayer sample can be found in table 1.1 together with physically plausible limits for each of the parameters. Due to the fact that the EUV reflectivity curve shown in Fig. 1.1 shows the first order Bragg peak of the layer system, none of the layers can be thicker than 7 nm, i.e. in the order of half of the wavelength. The barrier layers were designed to attain thicknesses below 1 nm. The densities of the various materials within this model was constrained to values between 50 % and 100 % with respect to their bulk density, while values above the bulk density are physically highly improbable. Due to the high peak reflectance of the multilayer sample in the EUV measurement, the maximum value of the Nevot-Croce factor was limited to be below  $\sigma \leq 2$  nm. With its upper limit, the measured peak reflectance can not be attained within this model thus not limiting the generality.

### The minimization functional and particle swarm optimization

As introduced above, the reconstruction of the model for the multilayer is an optimization problem. Based on the measured reflectivity data an optimization functional defines the goodness of the model with respect to the measured data. The quality is asserted based on the method of least squares [5, 11, 21] and the functional is defined as the reduced  $\tilde{\chi}^2$

$$\tilde{\chi}^2 = \frac{1}{M - P} \left[ \sum_m \frac{(I_m^{\text{model}} - I_m^{\text{meas}})^2}{\tilde{\sigma}_m^2} \right], \quad (1.1)$$

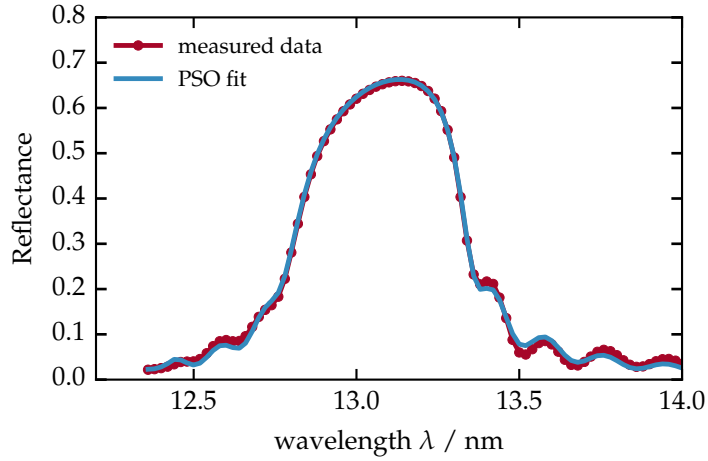
where  $M$  is the number of measurement points,  $P$  is the number of parameters used in the model,  $I_m^{\text{model}}$  is the calculated intensity for the corresponding measurement point with index  $m$  having the measured intensity  $I_m^{\text{meas}}$ . The calculated intensity for the EUV reflectivity curve above  $I_m^{\text{model}}$  follows directly from the matrix algorithm and the quantity  $R$  in Eq. (??) in chapter ?? . Each point is calculated based on the angle of incidence and wavelength associated with measurement point  $m$ . The experimental error for each measurement point is described by  $\tilde{\sigma}_m$ .

For the minimization of the functional in Eq. (1.1) we apply a global optimization algorithm known as PSO [19]. In contrast to the aforementioned gradient based methods, the particle swarm optimizer operates on the whole parameter space as defined by the upper and lower parameter limits, which are given in table 1.1 for the particular example here, without specific starting parameters influencing the convergence result. We implemented the PSO algorithm based on the draft by Carlisle and Dozier [7]. The basic mechanism of the algorithm is the definition of a swarm of individual particles, which are initialized randomly distributed across the allowed parameter space. Initially, each of those particles calculates the minimization functional at its random position retaining that result. In an iterative process, the global best solution (“social component”) found as well as the individual best solution (“cognitive component”) of each particle are used to calculate a velocity vector within the parameter space for each particle. Within that iteration each of the particle thus moves to a new position, where the minimization functional is again evaluated and compared the the individual and global best solutions. If a better value is found, the respective retained results are updated with the new value and the next iteration is performed. While following that process the particles eventually converge to the global best solution, which may or may not be the global best optimum of the whole optimization problem. Due to the combination of social and cognitive component, fast convergence into a local optimum can be avoided. The state of full convergence is reached, when either all particles occupy the same place in the parameter space or if stagnation is reached. Due to the statistical nature of the algorithm, convergence can not be guaranteed. Neither is the global best optimum found necessarily the global minimum. The result may be verified by repeated application of the algorithm or simply by reaching a satisfactory solution through comparison of the measured and calculated curves and thus the desired small  $\tilde{\chi}^2$  values.

### Model reconstruction based on the EUV reflectivity data

We have applied this optimization procedure to the Mo/B<sub>4</sub>C/Si/C sample and the measured EUV reflectivity curve. The fit result is shown together with the measured data in Fig. 1.3. The parameter results are listed in table 1.2. The solution does indeed provide

**Figure 1.3** | Theoretical reflectance curve based on the optimal model parameters obtained from the particle swarm optimization.



a very good agreement with the measured data. However, by repeated evaluation of the PSO procedure, significantly different results for the optimal parameter set with comparable agreement were found. Clearly, this is no desirable situation, since no definite answer of the actual thicknesses found in the sample can be made. To complete the characterization additional methods of model verification are thus required. We shall therefore discuss an additional approach to the optimization problem in the following section on how the model validity and the information content of the measured data can be asserted based on the example of the PSO results obtained here.

**Table 1.2** | Results for the optimized parameters based on the PSO of the EUV reflectivity for the Mo/B<sub>4</sub>C/Si/C sample.

Parameter	Definition	PSO result
$d_{\text{SiO}_2(\text{cap})}$ / nm	SiO <sub>2</sub> capping layer thickness	3.194
$d_{\text{Mo}}$ / nm	Mo layer thickness	2.460
$d_{\text{Si}}$ / nm	Si layer thickness	2.421
$d_{\text{C}}$ / nm	C buffer layer thickness	0.811
$d_{\text{B}_4\text{C}}$ / nm	B <sub>4</sub> C buffer layer thickness	1.308
$\sigma$ / nm	Névo-Croce parameter	0.322
$\rho_{\text{Mo}}$	Mo density w.r.t. bulk density	0.989
$\rho_{\text{Si}}$	Si density w.r.t. bulk density	0.883
$\rho_{\text{C}}$	C density w.r.t. bulk density	0.833
$\rho_{\text{B}_4\text{C}}$	B <sub>4</sub> C density w.r.t. bulk density	0.909

### 1.1.2 The Problem of Model Uniqueness and Maximum Likelihood Estimation

With the ambiguous reconstruction result of the previous section, the demand for a verification of the model with respect to the measured data becomes apparent. To clarify the problem of uniqueness of the solution it is instructive to investigate the influence of the individual model parameters on the theoretical reflectivity curve. In Fig. 1.4 we varied a subset of the parameters starting from the PSO solution from Sec. 1.1.1. In each of the subfigures, one parameter or a quotient of parameters is varied while all others are kept fixed. By comparison of Fig. 1.4a, 1.4b, 1.4c and 1.4e it becomes clear

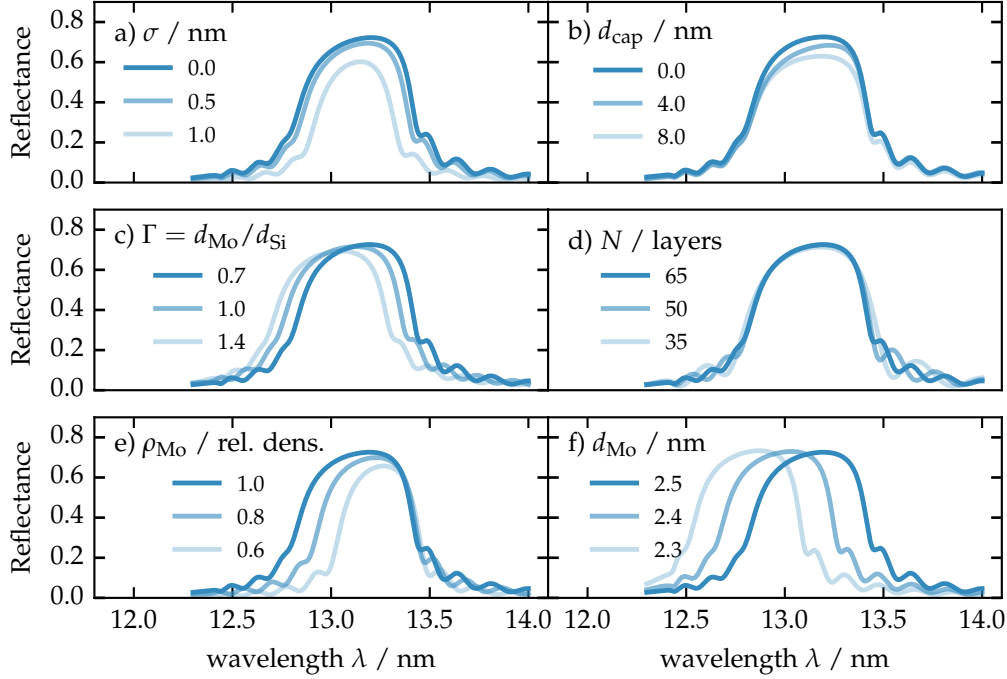


**Figure 1.4** | Parameter influence.

that a reduction of the peak reflectivity can originate in either a large roughness and interdiffusion parameter  $\sigma$  or similarly from the thickness of the capping layer, the silicon to molybdenum layer thickness ratio of the molybdenum density. A reconstruction based on a single EUV reflectivity therefore intrinsically produces a highly ambiguous result with strong parameter correlations. The available data, a single EUV reflectivity curve in this case, does not allow for a unique set of parameters of the model minimizing the  $\chi^2$  functional. In reality multiple solutions with equal values for  $\tilde{\chi}^2$  exist. Clearly, this raises the question of how accurately a reconstruction may be achieved here and requires to determine the value of  $\tilde{\chi}^2$  in vicinity of the PSO solution or possibly the whole parameter space.

### Maximum likelihood

We approach this problem of evaluating  $\tilde{\chi}^2$  across the parameter space by numerically sampling the functional based on a MCMC method [12]. An application of this technique to the design process of multilayer mirrors has been demonstrated by Hobson and Baldwin [18]. In our case, the match of model and experimental result is evaluated based on a non-centered  $\chi^2$  distribution assuming independent measurements. We further assume that any measured point is distributed around the actual reflectivity curve following a Gaussian distribution, i.e. we assume Gaussian errors for the experiment. The corresponding probability density function for a measurement result matching with the actual reflectivity curve, which is assumed to be obtainable exactly through the theoretical calculation, is then of Gaussian form [1]. Thus, the likelihood that the measured values match with the theoretical curve under the assumption that the model is correct is proportional to

$$L(E|M(\vec{x})) \propto \exp(-\tilde{\chi}^2(\vec{x})/2), \quad (1.2)$$

where  $E$  denotes the experiment, i.e. the measured data and  $M(\vec{x})$  represents the model given through parameter set  $\vec{x}$ , e.g. the parameters of the model in table 1.1. In our case however, we seek to evaluate the likelihood  $L(M(\vec{x})|E)$  that the model  $M(\vec{x})$  with a given set of parameters  $\vec{x}$  is valid assuming the experiment  $E$  yields the correct curve (the so called “posterior distribution”). Those two quantities are linked through the Bayesian theorem [4, 25] stating

$$L(M(\vec{x})|E) \propto L(E|M(\vec{x}))L(M(\vec{x})), \quad (1.3)$$

where  $L(M(\vec{x}))$  denotes the likelihood for the model to be valid for a specific set of parameters  $\vec{x}$  (the so called “prior distribution”). The prior distribution does contain any prior knowledge about the model and allowed parameters. For the example of the model parameters in table 1.1, the prior distribution is  $L(M(\vec{x})) \rightarrow -\infty$  for any parameter set outside the listed boundaries and  $L(M(\vec{x})) = 1$  everywhere else. In addition, we limit the maximum total period thickness, i.e. the sum of all layers in one period to only allow the appearance of the first Bragg peak within the measured spectral range through the same condition. Combining Eq. (1.2) and Eq. (1.3) then yields the likelihood functional

$$L(\vec{x}) = L(M(\vec{x})|E) \propto \exp(-\tilde{\chi}^2(\vec{x})/2)L(M(\vec{x})). \quad (1.4)$$

Solving the optimization problem posed in the previous section within this context is then, equivalently to the minimization of  $\tilde{\chi}^2$ , the maximization of the likelihood  $L(\vec{x})$ . The MCMC method poses a statistical approach on evaluating (mapping) the likelihood across the parameter space within the previously defined limits as in the PSO approach. It thus yields an alternative method on solving the optimization problem by extracting the maximum likelihood from the final result. However, in addition to the maximum value, the likelihood distribution in parameter space is obtained allowing to extract confidence intervals for each of the parameters [8]. Thereby, the aforementioned ambiguity of solutions can be quantified within the defined model and the available experimental data. The confidence intervals are defined as the one- or two-sigma standard deviations of the respective distributions for each parameter.

### Confidence intervals for the Mo/B<sub>4</sub>C/Si/C sample

We have applied an existing implementation of the MCMC algorithm by Foreman-Mackey et al. [10] to the EUV measurement of the Mo/B<sub>4</sub>C/Si/C sample in Fig. 1.1 with the model in Fig. 1.2. The likelihood as defined in Eq. (1.4) with the  $\chi^2$  functional from Eq. (1.1) is sampled in a high-dimensional space depending on the number of parameters in the model. We therefore need to project the distribution for each parameter by marginalizing over all other parameters. Alternatively, two-parameter correlations can be visualized by projecting on a two-dimensional area, again marginalizing across all other parameters. The projection for the Si and Mo layer thicknesses are shown in Fig. 1.5b and 1.5c. In both cases, a well defined distribution is obtained. In the two-dimensional projection in Fig. 1.5a, no correlations are apparent and a two-dimensional Gaussian-like shape results. In all cases, the one-sigma standard deviations for Gaussian distributions are shown

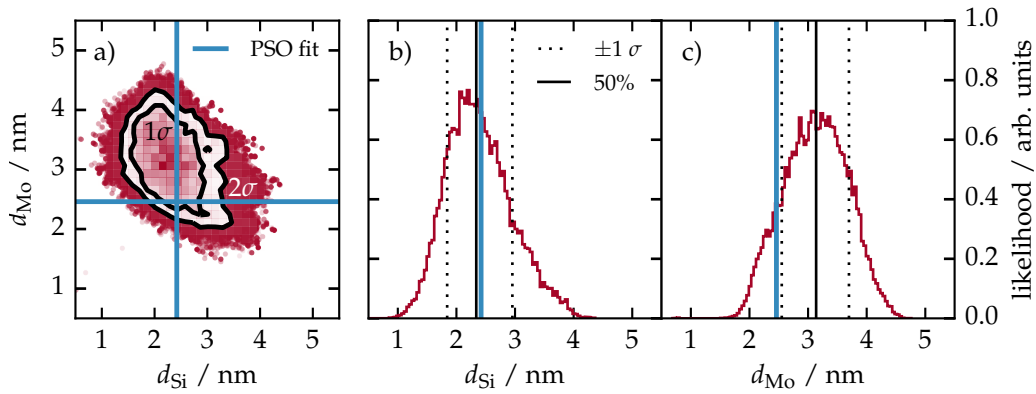


**Figure 1.5** | Results of the maximum likelihood estimation obtained via the MCMC procedure. a) Two dimensional projection of the likelihood distribution for the parameter pair  $d_{\text{Si}}$  and  $d_{\text{Mo}}$ . The projection was obtained by marginalizing over all other parameters of the model. The black contours indicate the areas for one and two standard deviations (one and two sigma contours). The blue lines in all three sub-figures indicate the best parameter set found with the PSO method. b) One dimensional projection of the likelihood distribution for the silicon layer thickness  $d_{\text{Si}}$ . The solid black line marks the center position (50% percentile) of the distribution. The dotted lines are the limits of one standard deviation. c) The one dimensional distribution similarly to b) for the molybdenum layer thickness.

together with the weighted center, i.e. the 50th percentile. The PSO result is also indicated, which is compatible with the one sigma standard deviation, but does not match the center of the likelihood result. The reason for that lies in higher order correlations of the parameters. In Fig. 1.6, all one-dimensional projections of the likelihood distribution are shown for all remaining parameters. Clearly, while a reasonably small confidence interval (again, one standard deviation for all distributions) can be found for the thickness of the carbon and boroncarbide layers, the off-center value for the silicon thickness of the PSO result in Fig. 1.5c is compensated by a larger than center value for the boroncarbide layer in Fig. 1.6. Thus, the thicknesses are correlated and are no independent model parameters. Nevertheless, confidence intervals can be obtained within the given model and the given prior (the boundaries listed in table 1.1 and are listed accordingly in table 1.3 for one and two standard deviations. Within the allowed boundaries, some parameters remain entirely undefined with equal likelihood for any parameter value, such as the SiO<sub>2</sub> capping layer thickness, the silicon, carbon and boroncarbide relative densities. Their corresponding total confidence intervals thus cover almost exactly 68.2% (one standard deviation) and 95.4% (two standard deviations) of the allowed respective

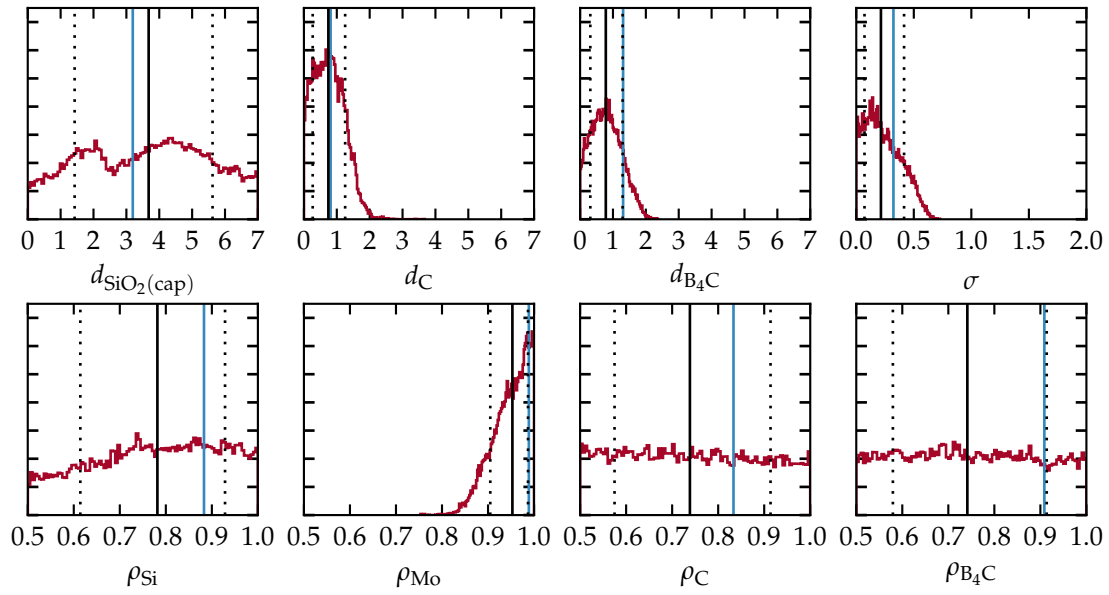


**Figure 1.6** | In analogy to Fig. 1.5b and 1.5c the one dimensional projections of the likelihood distribution estimation for the Mo/B<sub>4</sub>C/Si/C sample are shown for the remaining parameters of the model with the PSO result, the center value and one standard deviation.

parameter range. Hence, with respect to the model defined and the measured EUV reflectivity curve, no reliable value for those sample properties can be reconstructed.

**Table 1.3** | MCMC results obtained by the analysis of the EUV reflectivity for the Mo/B<sub>4</sub>C/Si/C sample. The center values (50% percentile) together with confidence intervals (c.i.) of one and two standard deviations are shown.

Parameter	PSO result	center value with $1\sigma$ c.i.	center value with $2\sigma$ c.i.
$d_{\text{SiO}_2(\text{cap})}$ / nm	3.194	3.677(−2.252/+1.944)	3.677(−3.407/+3.108)
$d_{\text{Mo}}$ / nm	2.460	3.137(−0.587/+0.560)	3.137(−1.054/+1.016)
$d_{\text{Si}}$ / nm	2.421	2.338(−0.497/+0.616)	2.338(−0.916/+1.294)
$d_{\text{C}}$ / nm	0.811	0.744(−0.477/+0.510)	0.744(−0.696/+0.971)
$d_{\text{B}_4\text{C}}$ / nm	1.308	0.782(−0.471/+0.511)	0.782(−0.722/+0.973)
$\sigma$ / nm	0.322	0.214(−0.143/+0.201)	0.214(−0.204/+0.347)
$\rho_{\text{Mo}}$	0.989	0.953(−0.048/+0.034)	0.953(−0.094/+0.045)
$\rho_{\text{Si}}$	0.883	0.782(−0.167/+0.147)	0.782(−0.264/+0.208)
$\rho_{\text{C}}$	0.833	0.739(−0.164/+0.175)	0.739(−0.228/+0.249)
$\rho_{\text{B}_4\text{C}}$	0.909	0.741(−0.162/+0.172)	0.741(−0.230/+0.247)

It should be noted, that although the aforementioned density values can not be determined based on the available data, they remain possibly highly correlated parameters. A valid optimization result can therefore only be obtained by either applying the PSO routine or by iterative application of the MCMC procedure, fixing single parameters according to their maximum likelihood value in the model and obtaining the resulting likelihood distributions for the remaining parameters according to that restricted model.

The results listed in table 1.3 serve as the model parameters for the analysis of diffuse scattering from the Mo/B<sub>4</sub>C/Si/C sample in chapter ?? below.



## 1.2 Molybdenum Thickness Variation in Mo/Si/C Multilayers

In the following we shall apply and extend the reconstruction procedure discussed in the above section to the problem of multilayer sample systems deposited with varying molybdenum layer thicknesses. For the engineering of a near-normal incidence mirror, the ratio of molybdenum layer thickness to total period thickness has a clear impact on the reflectivity curve as seen in Fig. 1.4c. Studies have shown, that an optimal value for high reflectivity is achieved by depositing 40% molybdenum layer thickness  $d_{\text{Mo}}$  with respect to the total period thickness  $D$  [3, 6]. During the deposition process, the layer of molybdenum grows in thickness and at a certain threshold, crystallites may begin to form [3, 30] inside the layer. Those may affect the interface morphology of the layer system at the boundaries to the molybdenum layer and possibly at further interfaces through correlation effects. This potentially increases the roughness and thus the loss of specularly reflected radiation. For the deeper understanding of those effects, we shall reconstruct the layer structure and determine the molybdenum layer thickness in each sample in comparison to the nominal values for the magnetron sputtering deposition.

### 1.2.1 Sample systems and experimental procedure

As a specific prototype for high-reflectance multilayer mirrors for the spectral range between 12.4 nm and 14.0 nm serve two sets of several samples of Mo/Si/C multilayer systems with C interdiffusion barriers with thicknesses of nominally below 0.5 nm at the Mo on Si interfaces (a detailed figure of the model for those samples is given below in Fig. 1.9 of the following sections). As mentioned above, the samples under investigation here were fabricated with increasing relative Mo thickness while keeping the nominal period thickness  $D \approx 7$  nm constant. In this study, we investigate two sets of samples. In the first set, the magnetron sputtered layers were deposited one after another for each sample. In the second set, during deposition, an additional polishing process was used once during sputtering each period to counteract the possible roughening due to the crystallization. The nominal values of the molybdenum layers in the two sample sets are listed in table 1.4.

nominal $d_{\text{Mo}}$ / nm (unpolished samples)	nominal $d_{\text{Mo}}$ / nm (polished samples)
1.70	1.70
1.85	1.85
2.00	2.00
2.15	2.15
2.30	2.30
2.45	2.45
2.60	2.60
2.75	2.75
2.90	2.90
-	3.05

**Table 1.4** | List of nominal molybdenum layer thicknesses in the two sample sets. Both sets were fabricated with a equidistant increase in thickness from 1.70 nm to 3.05 nm with 9 unpolished and 10 polished samples.

Spectrally resolved EUV reflectivity curves at an angle of incidence from the surface

normal of  $\alpha_i = 15^\circ$  and in the wavelength range from 12.4 nm to 14.0 nm have been measured for all samples at the EUVR beamline at the MLS. The data obtained is shown in Fig. 1.7 sorted by the nominal molybdenum layer thickness. The reflectivity curves in

**Figure 1.7** | a) Reflectivity curves for the unpolished samples across the wavelength at a fixed angle of incidence of  $\alpha_i = 15^\circ$  from the surface normal. The nine samples differ by the nominal Mo layer thickness indicated at the bottom axis. b) Reflectivity curves of the ten polished samples measured under the same conditions as for the first sample set.

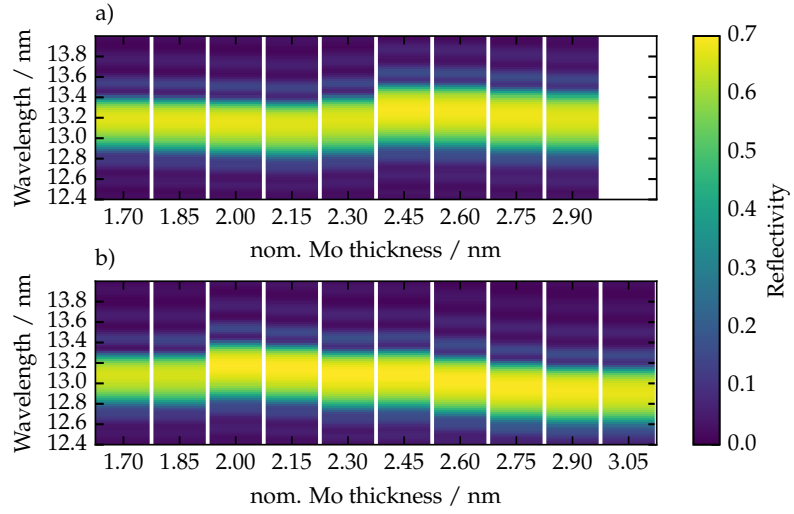
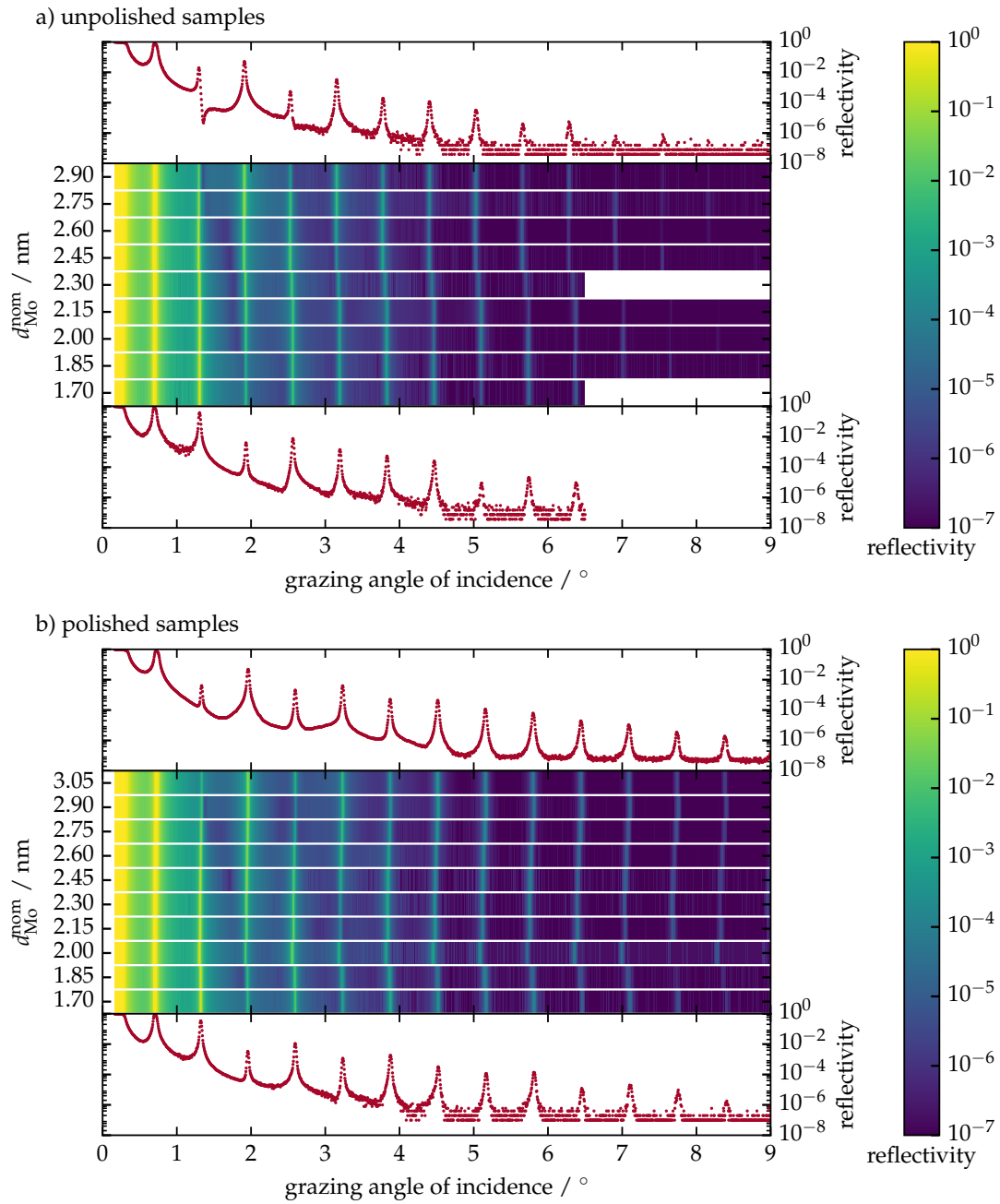


Fig. 1.7a and Fig. 1.7b have the characteristic curve shape of periodic EUV multilayer mirrors with a main broad maximum and side fringes, very similar to the mirror sample discussed in Sec. 1.1 above. In direct comparison of the measured reflectivity data, shifts of the peak center position are clearly visible. As illustrated in Fig. 1.4 above, several properties of a multilayer stack, e.g. molybdenum content and period thickness, contribute to such a difference. Clear differences in the peak reflectance value can also be observed in the two subfigures, with strong increases at  $d_{\text{Mo}}^{\text{nom}} = 2.45$  nm for the unpolished set and at  $d_{\text{Mo}}^{\text{nom}} = 2.00$  nm for the polished set. In all samples the only nominal difference, i.e. the only parameter changed during the deposition process, is the relative molybdenum thickness. The increase in reflectance and peak broadening are therefore indicators for an abrupt change in the multilayer properties.

For the purpose of obtaining additional information about the samples, in addition to the EUV reflectivity curves above, all samples were measured after deposition using a lab-based Cu- $K_\alpha$  hard x-ray diffractometer at the Fraunhofer IWS Dresden, Germany. The XRR data is shown in Fig. 1.8 for the set of unpolished and polished samples in direct comparison. The position of the Bragg peaks and their respective intensity contain additional information on the layer stack thicknesses and its interface properties. In both cases, shifts of the peak positions similar to those observed in the EUV curves become apparent. Especially the higher orders towards larger grazing incidence angles show distinct differences. In addition, in direct comparison of the XRR curves for the respective sample with  $d_{\text{Mo}}^{\text{nom}} = 3.05$  nm from the unpolished and polished sets (on the top of Fig. 1.8a and Fig. 1.8b), a higher intensity for higher-order Bragg peaks above grazing angles of incidence of  $\alpha_i^{\text{GI}} > 7^\circ$  can be observed for the polished sample. This hints towards an improved interface definition and sharpness due to the polishing process and consequently a lower roughness or interdiffusion.

In the following section we shall analyze the data discussed here to reconstruct a model of the samples using the MCMC approach introduced in Sec. 1.1 in order to verify the observations made here.



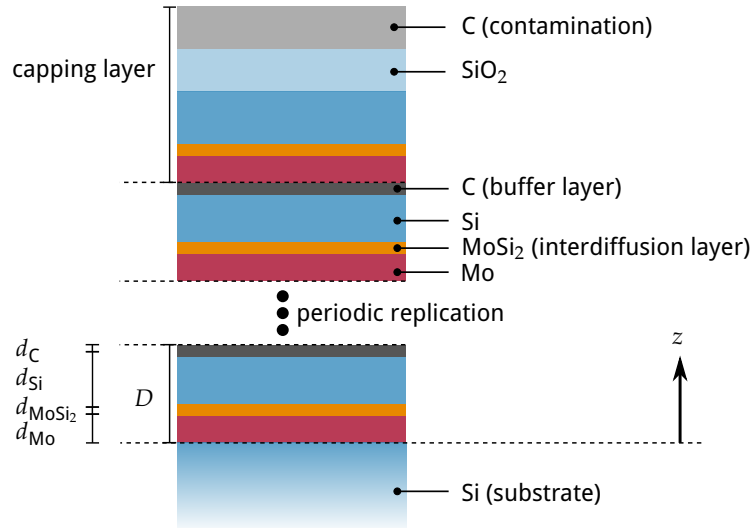
**Figure 1.8** | XRR data for all unpolished and polished samples shown in dependence on the nominal molybdenum layer thickness  $d_{\text{Mo}}^{\text{nom}}$ . In each of the subfigures a) and b) the XRR measurements for the sample with smallest and largest  $d_{\text{Mo}}^{\text{nom}}$  are shown on the bottom and the top of the subfigure, respectively. In between, the XRR curves are illustrated in as a color map plot.

## 1.2.2 Combined Analysis of X-ray and EUV reflectance

To obtain the actual layer thicknesses in the samples, we analyzed the data of the EUV reflectivity and XRR experiments and reconstructed these parameters by modeling and by combined analysis of the measured data. Both reflectivity curves are calculated by introducing a model for the multilayer system and applying the matrix formalism described in detail in the theory part of this thesis, Sec. ???. The model defined in the following paragraph is applied to both data sets.

The thicknesses of the Mo layers inside the stack were varied nominally from 1.7 nm to 3.05 nm from sample to sample, where the unpolished sample set lacks the last nominal thickness. The stacking of the different layers in the multilayer consists of the Mo and Si layers, as well as an additional C buffer layer at the Mo on Si interface to prevent interdiffusion. For the Si on Mo interfaces, no buffer layers were included since interdiffusion is usually less in this case [26]. However, for the theoretical description of the sample stack we consider an additional  $\text{MoSi}_2$  layer in the model, which is well known to form during the deposition process [3]. The full model used in the reconstruction is illustrated in Fig. 1.9 with the thickness parameters for each layer. To account for any

**Figure 1.9** | Model of the multilayer stack including the substrate and the capping layers. The periodic part is enclosed between the dashed lines with four layers in each period repeated 49 times. The capping period does not include an interdiffusion layer but has a natural  $\text{SiO}_2$  layer and a carbon-like layer accounting for contamination on the top surface.



contamination on the top sample surface, an additional carbon-like layer as the upper most layer was considered. In addition to the thicknesses of each layer we also allowed for a variation of the layer density between 80% and 100% of the bulk density. The model parameters and their boundaries entering in the optimization procedure are listed in table 1.5. Similar to the  $\text{Mo/B}_4\text{C/Si/C}$  in Sec. 1.1, a Névot-Croce damping factor was assumed to account for specular reflectivity loss due to interface imperfections.

**Table 1.5** | Parametrization of the Mo/Si/C multilayer samples with varying molybdenum layer thicknesses.

Parameter	Definition	Lower bound	Upper bound
$d_{\text{Mo}}$ / nm	Mo layer thickness	0.0	4.5
$d_{\text{Si}}$ / nm	Si layer thickness	0.0	7.0
$d_{\text{C}}$ / nm	C buffer layer thickness	0.0	0.6
$d_{\text{MoSi}_2}$ / nm	MoSi <sub>2</sub> interdiffusion layer thickness	0.0	0.6
$\sigma$ / nm	Nénot-Croce parameter (identical for all interfaces)	0.0	0.5
$\rho_{\text{Mo}}$	Mo density w.r.t. bulk density	0.8	1.0
$\rho_{\text{Si}}$	Si density w.r.t. bulk density	0.8	1.0
$\rho_{\text{C}}$	C density w.r.t. bulk density	0.8	1.0
$\rho_{\text{MoSi}_2}$	MoSi <sub>2</sub> density w.r.t. bulk density	0.8	1.0
Capping layer			
$d_{\text{C(cap)}}$ / nm	C capping layer thickness	0.0	3.0
$d_{\text{SiO}_2(\text{cap})}$ / nm	SiO <sub>2</sub> capping layer thickness	0.0	1.5
$\rho_{\text{C(cap)}}$	C density w.r.t. bulk density	0.0	1.0
$\rho_{\text{SiO}_2(\text{cap})}$	= $\rho_{\text{Si}}$ (identical to Si density)		

### Optimization functional and procedure

The data analysis was conducted similarly to the procedure described in Sec. 1.1. However, for the samples studied here, data from two separate experiments was measured with the goal to improve the reconstruction of the model. Due to the increased amount of data through the additional XRR measurements, a definition for a combined  $\chi^2$  functional is required to allow an analysis based on both data sets. The two data sets, i.e. the EUV and XRR reflectivity curves have significantly different number of points data points, which are not entirely independent of each other. In case of the XRR curve increasing the number of data points, e.g. by reducing the angular step size by half does not lead to better statistics due to systematic errors. Defining a  $\chi^2$  functional as the total sum of all measured data point residuals, i.e. both the EUV data and the XRR data would therefore create an unwanted weighting due to the large amount of XRR data points in comparison to far fewer EUV data points. To avoid this effect, we define the combined  $\chi^2$  functional as the sum of the reduced  $\tilde{\chi}^2$  functionals. The  $\tilde{\chi}^2$  is equivalently defined to Eq. (1.1) through,

$$\tilde{\chi}^2 = \frac{1}{M - P} \left[ \sum_m \frac{(I_m^{\text{model}} - I_m^{\text{meas}})^2}{\tilde{\sigma}_m^2} \right], \quad (1.5)$$

for each of the datasets separately. The reduced  $\tilde{\chi}^2$  can be interpreted as the average of the squared residuals of model prediction and experiment. Thereby, each experiment is reduced to a single comparable quantity. By the definition of

$$\chi^2 = \tilde{\chi}_{\text{EUV}}^2 + \tilde{\chi}_{\text{XRR}}^2, \quad (1.6)$$

we are therefore enabled to obtain confidence intervals for the parameters of the model, which represent a conservative (upper limit) estimation for the combined analysis of both

experiments, similarly to the procedure for a single EUV curve as described in Sec. 1.1 above. The combined  $\chi^2$  functional enters the likelihood through Eq. 1.4.

The solution to the inverse problem of reconstructing the optimal model parameters is conducted by minimizing the  $\chi^2$  functional (or equivalently maximizing the likelihood). To minimize the functional with respect to the best choice of parameters, we apply the MCMC method as described above for the Mo/B<sub>4</sub>C/Si/C sample system. We do not start with a PSO optimization, since the sample system is numerically simpler due to the decreased amount of layers and interfaces. The MCMC method itself yields an optimization result, although slower in convergence, as mentioned in the discussion of the procedure above in Sec. 1.1.2. As a starting point, again a random set of parameters is generated with respect to predefined boundaries listed in table 1.5. The limits are chosen in reference to prior knowledge and physical plausibility. Confidence intervals for each value within the underlying model are estimated from the likelihood distribution resulting from the MCMC as one standard deviation of the sample distribution in each parameter.

We shall discuss the results of the optimization procedure at the example of the unpolished sample with nominal molybdenum layer thickness of  $d_{\text{Mo}}^{\text{nom}} = 3.05$  nm. The results of the MCMC maximum likelihood estimation for the other samples were found to show the same properties and the same findings discussed in the following with the only distinction of broader or even improved distributions in some cases. The latter causes the confidence intervals to be different for the respective parameters. The reason for the broader likelihood distribution is clearly a decreased applicability of the model in some cases possibly due to changes through crystallization. Nevertheless, the model still shows sufficiently good agreement with the data.

As a first step, the MCMC procedure was performed within the defined boundaries for all parameters. An unambiguous result was only found with respect to the thickness parameters of Mo, with the smallest confidence intervals in comparison to all other parameters, and Si, as well as for the Névot-Croce parameter  $\sigma$ , whereas all other parameters show broad likelihood distributions within the predefined boundaries not allowing a unequivocal parameter determination. Therefore, the best model was obtained in a two-step process. First the MCMC optimization was performed including all parameters as mentioned above. Proceeding from this, the value of the Mo thickness with its confidence interval was obtained by marginalizing over all other parameters, yielding the most precise parameter estimation from the procedure. The results for the molybdenum and silicon layer thickness parameters are shown in Fig. 1.10. In comparison

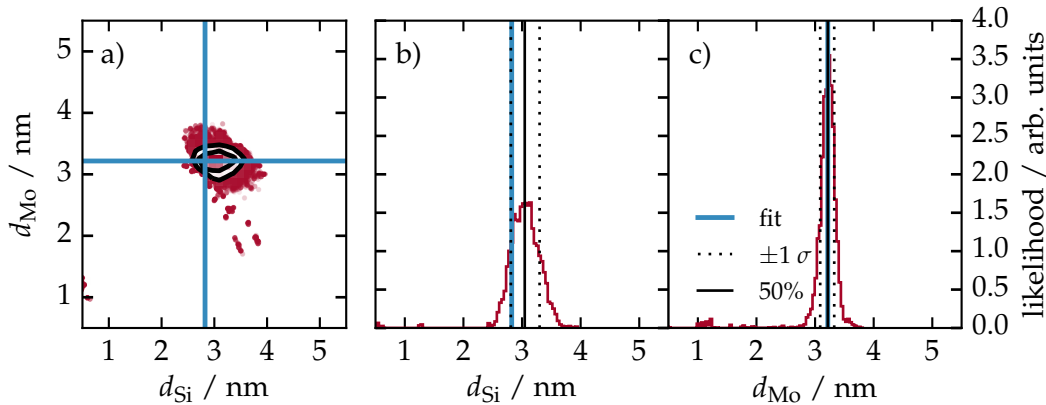
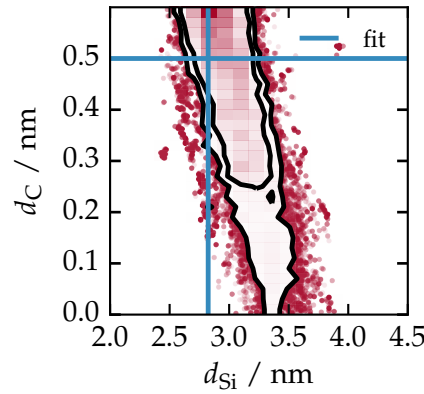


Figure 1.10 | Combined analysis

to the analysis based on only EUV data for the Mo/B<sub>4</sub>C/Si/C in Fig. 1.5, the inclusion of additional XRR measurements lead to significantly smaller confidence intervals and thus higher accuracy of the reconstruction, although the two systems have a limited comparability due their different layer layouts. The method of combining the analysis of two datasets of EUV and XRR measurements has been previously applied by others [31], which have come to the same result of a significantly improved model reconstruction.

In a second step, another MCMC optimization was performed on a reduced parameter set, fixing the determined molybdenum layer thickness to its optimal value, i.e. the 50% percentile of its distribution. Finally, the layer thicknesses of the C barrier layer and the MoSi<sub>2</sub> interdiffusion layer were fixed to their nominal values of  $d_C = d_{\text{MoSi}_2} = 0.5$  nm. Due to the broad distribution result for the likelihoods of those parameters, this comes without a limitation of the generality for this analysis, since any value is valid within the predefined boundaries. Additionally, this ensures comparability of the models for all samples without constraining the applicability of the model with respect to the data available.



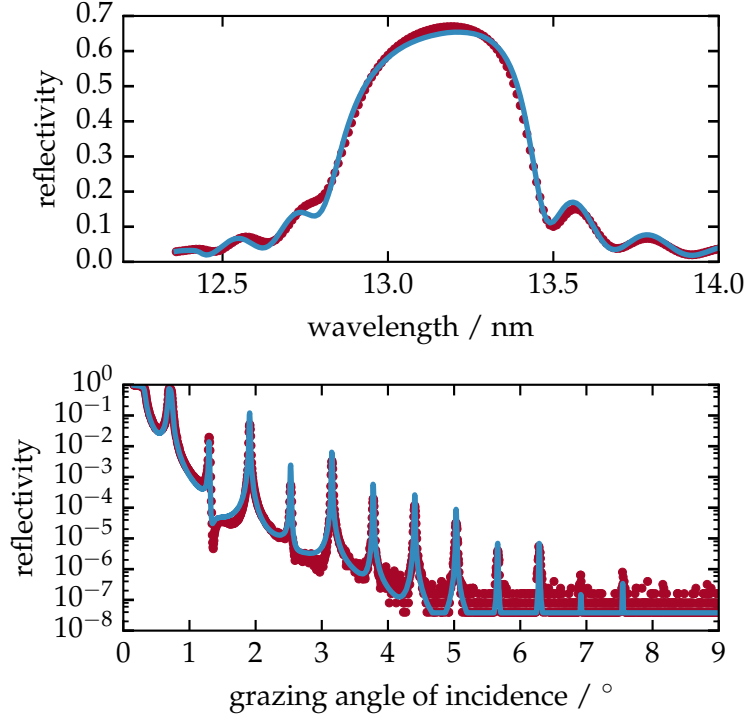
**Figure 1.11** | Two-dimensional likelihood distribution indicating the correlation of silicon and carbon layer thickness. The distribution was obtained by marginalizing over all remaining parameters of the model. The blue lines indicate the fit obtained through the two-step MCMC optimization procedure (see main text).

The results of the second MCMC procedure of the restricted model yield the remaining values for the model parameters by obtaining the globally best solution found. The final result is indicated by the blue solid lines in Fig. 1.10. Due to the choice to restrict the model to a buffer layer thickness of  $d_C = 0.5$  nm, we find the optimal solution for the silicon layer thickness at the limit of one standard deviation in Fig. 1.10b. The distributions shown represent the MCMC results of the unrestricted model, where the silicon and carbon layer thicknesses are strongly correlated as shown in Fig. 1.11. By restricting the carbon layer thickness to its nominal value, this correlation is resolved and the corresponding silicon layer thickness is well within the interval of one standard deviation as indicated through the solid black contours in Fig. 1.11.

### 1.2.3 Optimization results

The theoretical reflectivity curves calculated from the optimal model parameters for the unpolished sample with  $d_{\text{Mo}}^{\text{nom}} = 3.05 \text{ nm}$  are shown in Fig. 1.12. Overall, a very good agreement of the two experiments with the theoretical curve are obtained. The full list for

**Figure 1.12** | Experimental data in comparison with the theoretical curves calculated with the model parameters obtained from the combined analysis of EUV and XRR data. The data shown here was measured on the unpolished sample with nominal molybdenum thickness of  $d_{\text{Mo}}^{\text{nom}} = 3.05 \text{ nm}$ .



all molybdenum layer thicknesses for all samples and the respective confidence intervals in comparison to their nominal layer thickness are given in table 1.6.

**Table 1.6** | List of nominal molybdenum layer thicknesses in the two sample sets. Both sets were fabricated with an equidistant increase in thickness from 1.70 nm to 3.05 nm with 9 unpolished and 10 polished samples.

nom. $d_{\text{Mo}}$ / nm	EUV & XRR (unpolished)	EUV & XRR (polished)
1.70	1.81(−0.12/+0.24)	1.77(−0.22/+0.19)
1.85	1.98(−0.15/+0.14)	1.91(−0.12/+0.17)
2.00	2.08(−0.11/+0.22)	2.29(−0.28/+0.13)
2.15	2.31(−0.22/+0.21)	2.45(−0.43/+0.06)
2.30	2.43(−0.09/+0.16)	2.60(−0.12/+0.14)
2.45	2.68(−0.13/+0.16)	2.58(−0.21/+0.15)
2.60	2.91(−0.17/+0.12)	2.87(−0.22/+0.12)
2.75	3.02(−0.15/+0.15)	3.03(−0.16/+0.14)
2.90	3.22(−0.13/+0.11)	3.15(−0.13/+0.13)
3.05	-	3.47(−0.19/+0.13)

The optimal parameters for the molybdenum layer thickness  $d_{\text{Mo}}$  and the period thickness  $D$  found for both sample sets in the two-step MCMC analysis are shown in Fig. 1.13. The confidence intervals shown in Fig. 1.13a are one standard deviation of the likelihood determined for the Mo layer thickness by the first-step MCMC procedure, i.e. for the unrestricted model with the parameter limits as listed in table 1.5. The results show the desired linear increase in molybdenum layer thickness, however at a systematically higher thickness than the nominal values. A possible cause for that



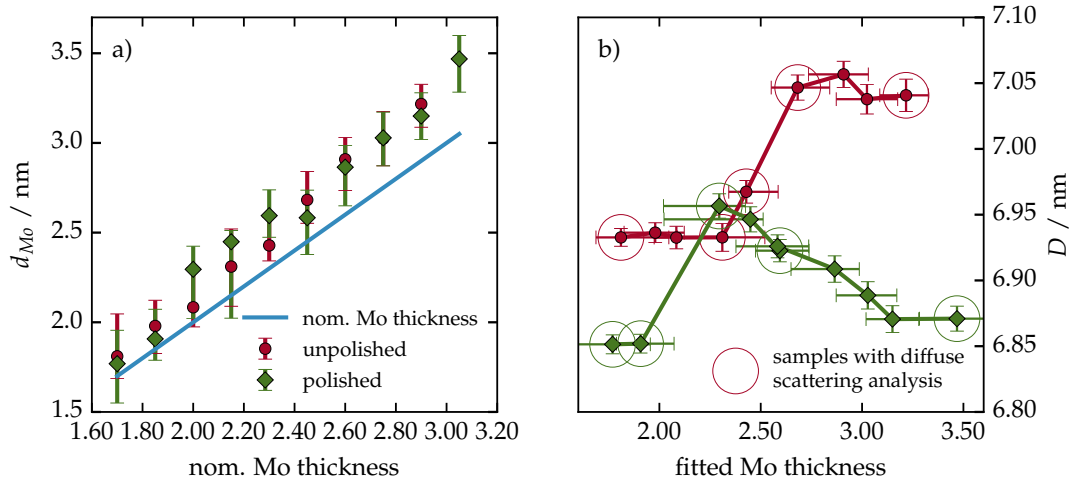
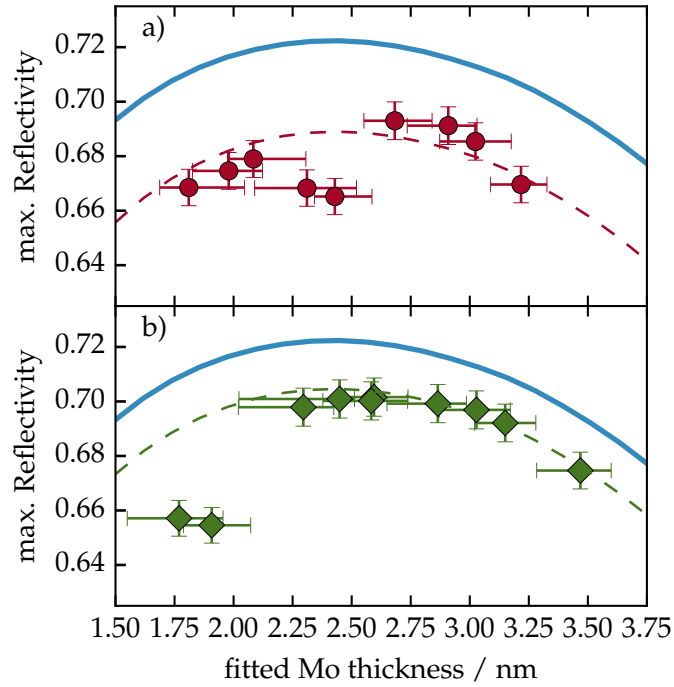


**Figure 1.13** | a) Fitted Mo thickness values for both sample sets resulting from the MCMC analysis (see text). The nominal Mo layer thickness is shown in good agreement with the obtained thicknesses. b) Fitted total period thickness  $D$  for both sample sets. For both sample sets, clear jumps can be observed at approx.  $d_{Mo}^{nom} = 2.00$  nm and  $d_{Mo}^{nom} = 2.38$  nm, respectively, which is attributed to the crystallization threshold (see text). The marked (circle) samples were measured and analyzed with respect to the diffuse scattering.

observation, consistent with the model reconstruction results, is the possible interdiffusion of the molybdenum layer with the silicon and carbon during deposition. This would reduce the relative density of the molybdenum layer. The reconstruction results for all samples indeed show systematically reduced density values of  $\rho_{Mo} \approx 90\%$  w.r.t. the Mo bulk density. Thus, the nominal amount of deposited molybdenum leads to higher thicknesses than desired. In Fig. 1.13b the fitted period thicknesses  $D$  are shown in dependency of the fitted molybdenum thicknesses.

For both sets, distinct jumps can be observed between  $d_{Mo} \approx 1.9$  nm and  $d_{Mo} \approx 2.3$  nm for the polished samples and between  $d_{Mo} \approx 2.3$  nm and  $d_{Mo} \approx 2.7$  nm for the unpolished set. To better understand this observation, Fig. 1.14 shows the maximum peak reflectance of all EUV measurements also as a function of the reconstructed Mo layer thickness. The identical blue solid line in both subfigures indicates the maximum peak reflectance attainable for a perfect multilayer system with the respective Mo layer thickness without any interdiffusion or roughness. For the calculation a carbon capping layer of  $d_{C(cap)} = 2.0$  nm and a relative density of  $\rho_{C(cap)} = 0.5$  and a silicon dioxide layer of  $d_{SiO_2} = 2.0$  was considered. The dashed curves in both figures show the expected maximum peak reflectance values for the two sample systems calculated by adding the respective roughness/interdiffusion to the model and varying the molybdenum thickness accordingly. In both cases, a significant dip with respect to the expected value can be observed starting at thicknesses of  $d_{Mo} = 2.31(-0.22/+0.21)$  nm for the unpolished samples in Fig. 1.14a and at  $d_{Mo} = 1.77(-0.22/+0.19)$  nm for the polished samples in Fig. 1.14b. We attribute this significantly diminished peak reflectance to the process of crystallization as the most likely cause. These values are consistent with the increase observed in the period thickness for both cases. However, the jump in the period thickness value with the increasing molybdenum layer thickness is observed one (in case of the unpolished samples) to two data points (in case of the polished samples) after the first dip in peak reflectance. Possibly, the deposition is affected by the crystallization threshold causing the increase in period thickness. The values measured here for the dip in peak

**Figure 1.14** | Peak reflectance values for each sample obtained from the EUV measurements for the unpolished sample set (a) and the polished sample set (b). The maximum theoretical reflectance is shown in both subfigures for a perfect (no roughness or interdiffusion) layer system with the same specifications as the samples.



reflectance is in agreement with earlier observation of molybdenum crystallization in literature [3] for the unpolished samples set. The polishing process shifts that threshold to lower thicknesses by approximately 0.2 nm to 0.3 nm.

For a deeper investigation of the interface morphology during the presumed crystallization threshold, EUV diffuse scattering experiments have been conducted for selected samples of the respective set. The selection is marked with open circles in Fig. 1.13. To gain a deeper understanding of the reflectivity dip and the period increase, the samples in vicinity of this feature in the Fig. 1.14 and Fig. 1.13 were investigated in comparison to reference samples above and below the threshold. This analysis is the topic of chapter ?? of this thesis and described and discussed in detail there based on the reconstruction results obtained here.

### 1.3 Analysis of Cr/Sc Multilayers with Sub-nanometer Layer Thickness

In the previous sections we have characterized multilayer systems specifically designed to reflect radiation in the EUV spectral range from 12.5 nm to 14.0 nm wavelength. There, the three to four layer systems per period with period thicknesses of  $D \approx 7$  nm were used to achieve constructive interference at the desired reflection angles. We shall now expand the analysis to a different system. Multilayer mirrors designed to reflect radiation in the spectral range between 2.2 nm and 4.4 nm wavelength, the so called *water window*. Those systems share the basic principle of a one-dimensional Bragg crystal with the Mo/Si multilayer stacks from the previous sections, but differ in the selection of materials. The intrinsic relationship between spectral range and period thickness to achieve constructive interference, requires period thicknesses of  $D \approx 1.5$  nm for this case and higher period replication.

The system we focus on in the rest of this chapter is composed out of a bilayer stack

of chromium (Cr) and scandium (Sc). A detailed description of the sample preparation process and the choice of the layer materials can be found in Ch. ??, Sec. ?. The sample is optimized to reflect radiation of  $\lambda = 3.14 \text{ nm}$  at an angle of incidence of  $\alpha_i = 1.5^\circ$ . Its periodicity is  $N = 400$  bilayer periods, where the last period has a larger Cr capping layer thickness. The model of the sample is shown in Fig. 1.15. The small period thickness

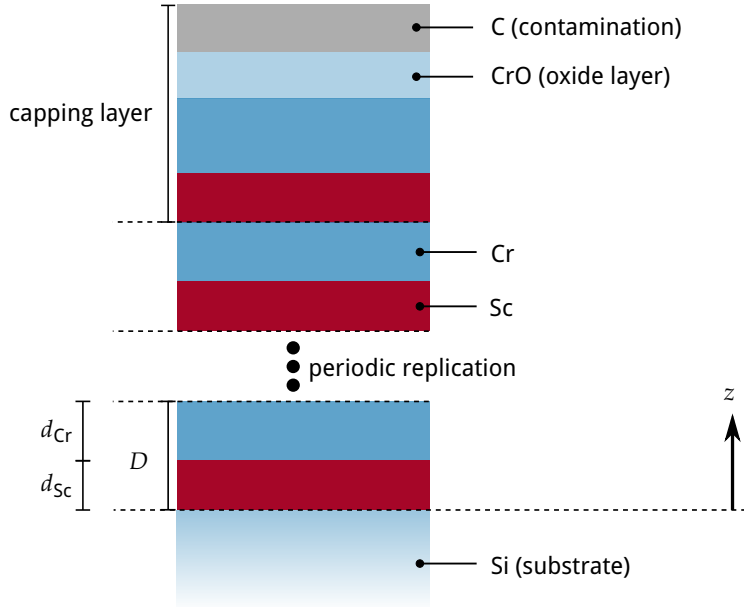


**Figure 1.15** | Model of the multilayer stack including the substrate and the capping layers. The periodic part is enclosed between the dashed lines with four layers in each period repeated  $N = 64$  times. The capping period does not include an interdiffusion layer but has a natural  $\text{SiO}_2$  layer.

of only  $D \approx 1.5 \text{ nm}$  for this type of sample yields individual layer thicknesses in the sub-nanometer regime, for a bilayer period with approximately equal individual layer thicknesses. This is a significant difference to the Mo/Si systems treated in the beginning of this chapter, where the molybdenum and silicon layers were well above  $> 1.7 \text{ nm}$ , even in the smallest case existed. The buffer and interdiffusion layers, which nominally have thicknesses in the same order of magnitude as expected for the Cr/Sc system, could not be characterized based on the methods employed above. We shall therefore first compare the results obtained with an approach similar to the methods in the previous sections to establish a limit to the applicability of discrete layer models.

### 1.3.1 Reconstruction with a discrete layer model approach

In analogy to Sec. 1.2, we seek to reconstruct the individual layer thicknesses based on experimental data. For this we construct a discrete layer model as illustrated in Fig. 1.15 in analogy to the procedure applied for the Mo/Si multilayer systems. The parameters of this discrete layer model are listed in table 1.7 together with the upper and lower bound for the particle swarm optimization procedure.

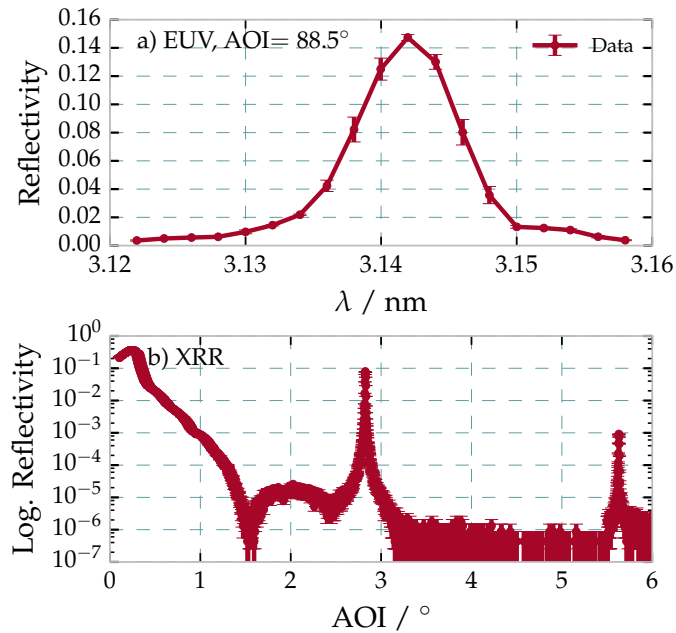
The reflectivity of the sample in the water window spectral range from  $3.12 \text{ nm}$  to  $3.16 \text{ nm}$  was measured at the soft x-ray beamline (SX700) beamline at electron storage ring for synchrotron radiation (BESSY II). The angle of incidence was  $\alpha_i = 1.5^\circ$  (corresponding to a grazing angle of incidence of  $\alpha_i^{\text{GI}} = 88.5^\circ$ ), which corresponds to the design goal for this mirror prototype. In addition, similar to the Mo/Si samples, a XRR measurement was conducted in the DESY laboratory using a laboratory-based X-ray diffractometer (X'Pert PRO MRD, Panalytical). The diffractometer is equipped with a high-resolution goniometer and uses  $\text{Cu-K}_\alpha$  radiation. The XRR intensities were recorded using a PIXcel

**Table 1.7** | Parametrization of the Cr/Sc binary multilayer model.

Parameter	Definition	Lower bound	Upper bound
$d_{\text{Cr}}$ / nm	Cr layer thickness	0.0	1.5
$d_{\text{Sc}}$ / nm	Sc layer thickness	0.0	1.5
$\sigma$ / nm	Nénot-Croce parameter (identical for all interfaces)	0.0	0.5
$\rho_{\text{Cr}}$	Cr density w.r.t. bulk density	0.5	1.0
$\rho_{\text{Sc}}$	Sc density w.r.t. bulk density	0.5	1.0
Capping layer			
$d_{\text{C (cap)}}$ / nm	C capping layer thickness	0.0	1.0
$d_{\text{CrO (cap)}}$ / nm	SiO <sub>2</sub> capping layer thickness	0.0	1.5
$d_{\text{Cr (cap)}}$ / nm	SiO <sub>2</sub> capping layer thickness	0.0	3.0
$\rho_{\text{C (cap)}}$	C density w.r.t. bulk density	0.0	1.0
$\rho_{\text{CrO (cap)}}$	CrO density w.r.t. bulk density	0.0	1.0
$\rho_{\text{Cr (cap)}}$	Cr (cap) density w.r.t. bulk density	0.5	1.0

counting detector. The dynamic range achieved in the measurements extended down to a reflectance of  $10^{-6}$  for grazing angles of incidence of  $\alpha_i = 0^\circ$  to  $\alpha_i = 3^\circ$ .

Both measurement curves are shown together in Fig. 1.16. Due to the short period of

**Figure 1.16** | EUV and XRR


the multilayer sample, only two Bragg peaks could be observed in this angular range. All higher order peaks were below the detection threshold of  $10^{-6}$  in reflected intensity. The dominating experimental uncertainty was the inhomogeneity of the sample stack across the sample area. The given uncertainty values for each of the measurement points were estimated, by measuring the peak reflectance on positions marking a cross of 2 mm by 2 mm in the sample center. This data was compared to theoretical expectance value based on a PSO fit of the discrete layer model above for the EUV curve (for details of the optimization results see below). From this a drift of the period thickness  $D$  was obtained

and uncertainties were calculated as the difference of two theoretical curves attaining the maximum and minimum  $D$  values. Similarly, uncertainties for the XRR curves were calculated by simulating theoretical curves based on the same period drifts.

In comparison, the most remarkable difference with respect to the Mo/Si mirrors is the significantly reduced peak reflectance of the EUV curve in Fig. 1.16a compared to the curves in Fig. 1.1 and Fig. ??c. The maximum value attained is only approximately  $R_{\max} \approx 15\%$  while it is up to  $R_{\max} \approx 70\%$  for the Mo/Si systems. The reasons for this are the different spectral range and the material properties at the water window wavelengths.

To better illustrate the differences to the Mo/Si systems, we have conducted an analysis based on the discrete layer model of a Cr/Sc multilayer as described above. The particle swarm optimization was done based on the EUV data shown in Fig. 1.16a and the parameters and limits listed in table 1.7. The resulting parameters are listed in table 1.8. The capping layer results were obtained in a combined PSO analysis based on the EUV

Parameter	PSO result
$d_{\text{Cr}} / \text{nm}$	0.8224
$d_{\text{Sc}} / \text{nm}$	0.7510
$\sigma / \text{nm}$	0.375
$\rho_{\text{Cr}}$	0.876
$\rho_{\text{Sc}}$	0.957
Capping layer	
$d_{\text{C (cap)}} / \text{nm}$	0.462
$d_{\text{CrO (cap)}} / \text{nm}$	1.143
$d_{\text{Cr (cap)}} / \text{nm}$	2.322
$\rho_{\text{C (cap)}}$	0.502
$\rho_{\text{CrO (cap)}}$	0.618
$\rho_{\text{Cr (cap)}}$	0.851

**Table 1.8** | PSO fit results for the discrete layer Cr/Sc multilayer model. The bulk multilayer parameters were obtained by exclusively applying the PSO method to the EUV data. The capping layer parameters were deducted from the XRR data excluding the Bragg peaks in a combined analysis.

and XRR data excluding the areas of the Bragg peaks. This grazing incidence reflectivity data has a very high sensitivity for the top surface layers, which can not be deducted from an EUV curve alone as demonstrated in Sec. 1.1.

The theoretical curve obtained from the PSO procedure is shown in Fig. 1.18 in direct comparison with the theoretically achievable maximum reflectivity curve. The latter was obtained by calculating the resulting reflectivity based on the parameter results in table 1.8, but without any roughness or interdiffusion, i.e. by requiring  $\sigma \equiv 0.0$ . The Sc to Cr ratio was found to be  $\Gamma_{\text{Sc}} = d_{\text{Sc}}/d_{\text{Cr}} = 0.48$  with a high root mean square (r.m.s.) value of  $\sigma = 0.385 \text{ nm}$  for the Névod-Croce factor. While the EUV reflectance curve shows excellent agreement with the measured data, there is a significant offset to the theoretically achievable maximum reflectance. For the particular model derived above, theoretical reflectance values of  $R_{\max} > 50\%$  are possible. This large difference, especially compared to Mo/Si systems which are very close to the theoretically achievable maximum reflectance (cf. Fig. 1.14), hints at strong roughness or intermixing of the two materials. To verify the applicability of the discrete (binary) layer model used here, the calculated curves for both experiments, the EUV and XRR curve, are shown together in Fig. 1.18.

Again, the EUV data is matched excellently, while in the case of the XRR measurement the first Bragg peak is found to be matched by the model also in the hard x-ray regime.

**Figure 1.17** | Fitted experimental EUV reflectance curves across the wavelength of the radiation impinging at  $\alpha_i = 1.5^\circ$  from normal, based on the binary model. The green curve shows the maximum possible reflectance assuming a perfect multilayer system without roughness or interdiffusion.

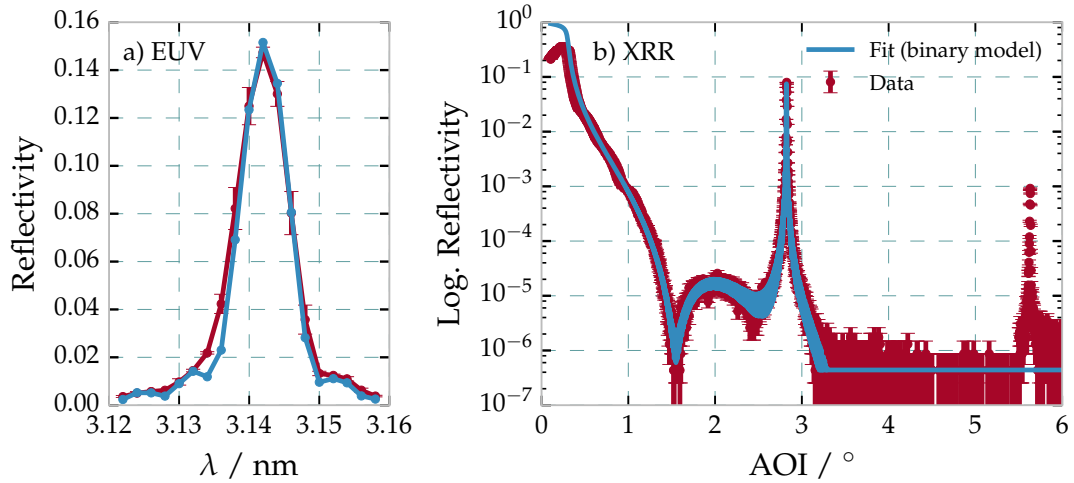
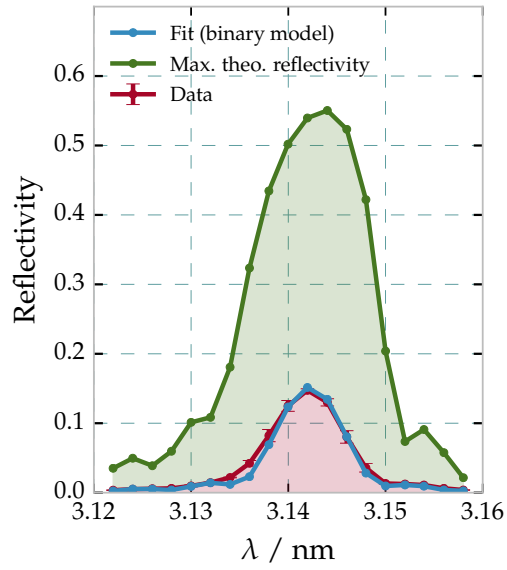


**Figure 1.18** | a) Measured EUV reflectivity curve for and near-normal angle of incidence of  $\alpha_i = 1.5^\circ$  together with calculated curve of the PSO-based binary model reconstruction. b) Measured and calculated XRR curves for the same sample and model parameters at grazing angles of incidence using radiation at the Cu-K $\alpha$  wavelength. A clear mismatch of the theoretical curve and the measured data can be observed for the second Bragg peak between  $\alpha_i^{\text{GI}} = 5.0^\circ$  and  $\alpha_i^{\text{GI}} = 6.0^\circ$ .

However, the second Bragg resonance, clearly visible with a peak reflectance value of approximately  $10^{-3}$  is not represented by the model at all. A fully combined analysis similarly to the approach in Sec. 1.2 could not yield a consistent result. The r.m.s. value for  $\sigma$  required to reduce the theoretical EUV reflectance down to the measured level could not be brought into agreement with the XRR curves second Bragg peaks appearance. In a strictly binary model like this one with a layer thickness ratio of  $\Gamma_{\text{Sc}} \approx 0.5$ , the second Bragg peak is additionally suppressed due to symmetry reasons. Thus, there is a clear mismatch of the model reconstruction and the experimental observations, mostly due to the complementary data delivered through the measurement of the second Bragg peak of the XRR curve. This is a strong indicator, that the simple model as defined above does not suffice to describe the physical situation of the sample. Therefore, a more elaborate model is required introducing additional parameters to account for the increased complexity of the samples layer properties compared to the Mo/Si sample systems above.

### 1.3.2 Extending The Model to Graded Interfaces and Interdiffusion

The physical situation of Cr/Sc multilayer systems with individual layer thicknesses in the sub-nanometer regime is significantly different than in comparably large thicknesses of several nanometers such as in the Mo/Si case of the two preceding sections. It is well known [28], that magnetron sputtered Cr and Sc multilayer systems, similarly to the Mo/Si systems, suffer from imperfect interfaces. The main reason for that is interdiffusion of the two materials into each other. In addition, roughness at the interfaces exists and further diminishes an ideal chemically abrupt transition from one material to the next. Due to the small layer thicknesses required to achieve the first Bragg resonance upon near-normal incidence with radiation of  $\lambda = 3.14 \text{ nm}$ , roughness and interdiffusion may occur over an interdiffusion zone as large as the total layer thickness itself. The results from the specular EUV and XRR measurements shown above, clearly demonstrate that a binary model with only a Névot-Croce damping parameter  $\sigma$  does not provide an accurate model for the physical reality. Instead, a more complex model is required. Here, we define a periodic model, repeated in units of one bilayer period, to account for possible interdiffusion gradients and intermixing between the two materials in the stack. The symmetry of two identically thick layers within one period in the simple model above leads to a suppression of the second order Bragg peak. Nevertheless, physically this symmetry effect can be broken by accounting for interdiffusion zones with different thicknesses, depending on whether Cr was deposited on Sc or vice versa. Thereby, the second Bragg peak is no longer suppressed even though both layers have the same thickness if the interdiffusion zones are asymmetric. Physical causality further dictates, that the two layers intermix gradually. The model, which we use to reconstruct the Cr/Sc multilayer sample measured above is illustrated in Fig. 1.19 in direct comparison to the simple model used before. The interdiffusion zones are modeled following a sinusoidal profile, which represents a smooth transition from the refractive index of the Cr layer to the Sc layer and vice versa. The thickness of those zones is given by the parameters  $s_{\text{Sc}}$  and  $s_{\text{Cr}}$ . For the calculation of the electromagnetic fields inside the stack, the interface region is sampled with a fixed number of equally spaced points in  $z$ -direction, effectively creating a region of thin sublayers with a gradually changing index of refraction (illustrated by the red stepped function in Fig. 1.19). To take into account intermixing extending across the full period, we introduced an intermixing parameter  $\eta$ . The effective indices of refraction of the individual Cr and Sc layers are then given

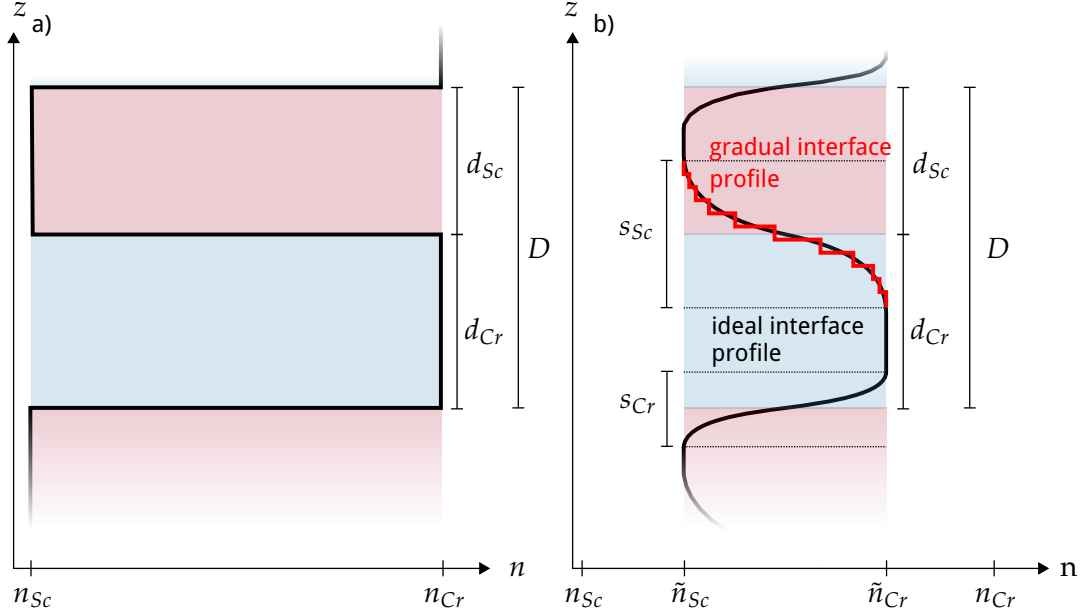


**Figure 1.19** | a) Binary Cr/Sc multilayer model with total period thickness  $D$  and the individual layer thicknesses  $d_{Sc}$  and  $d_{Cr}$ . b) Model with explicit gradual interfaces following a sinusoidal profile. The ideal interface profile is approximated through discrete sublayers as indicated in red, forming the actual gradual interface profile entering the electric field calculations. The thickness of the interdiffusion zones can differ for the top and bottom interface in each period. Their total thicknesses are given by  $s_{Sc}$  and  $s_{Cr}$ . The effective index of refraction for both layers is given by  $\tilde{n}_{Sc}$  and  $\tilde{n}_{Cr}$ , respectively.

through

$$\begin{aligned}\tilde{n}_{Cr} &= (\eta/2)n_{Sc} + (1 - \eta/2)n_{Cr}, \\ \tilde{n}_{Sc} &= (1 - \eta/2)n_{Sc} + (\eta/2)n_{Cr}, \\ \text{for } \eta &\in [0, 1],\end{aligned}\tag{1.7}$$

where  $n_{Cr}$  and  $n_{Sc}$  are the tabulated values [17] with densities  $\rho_{Cr}$  and  $\rho_{Sc}$ .

With the definition of the model as outlined above, natural restrictions arise for the parameters. As an example, the interdiffusion zone region can not extend across half of the thickness of the original layers total thickness described by the parameter  $d_{Cr}$  or  $d_{Sc}$ , respectively. Instead, the intermixing parameter would have to be increased to account for that situation. The model is therefore parameterized according to the list of effective parameters given in table 1.9 together with their allowed ranges for the optimization procedure in analogy to the analysis conducted in the previous sections. The range limits arise either from physical plausibility or are intrinsic properties of the parameter definition. Here,  $D$  is the full period thickness,  $d_{Sc}$  and  $d_{Cr}$  are the nominal layer thicknesses of the Cr and Sc layers as indicated in Fig. 1.19, and  $\rho_{Sc}$  and  $\rho_{Cr}$  their respective densities with respect to their bulk densities  $\rho_{Sc}^* = 2.989 \text{ g/cm}^3$  and  $\rho_{Cr}^* = 7.19 \text{ g/cm}^3$  [17]. The loss of specular reflectance due to roughness-induced scattering is considered through the Névet-Croce factor using  $\sigma_r$  identical at each interface. This is necessary to



**Table 1.9** | Multilayer parametrization and parameter limits

Parameter	Definition	Lower bound	Upper bound
$D$ / nm	$= d_{\text{Sc}} + d_{\text{Cr}}$	1.5	1.6
$\Gamma_{\text{Sc}}$	$= d_{\text{Sc}}/D$	0.0	1.0
$s_d$ / nm	$= s_{\text{Sc}} + s_{\text{Cr}}$	0.0	1.6
$\Gamma_s$	$= s_{\text{Sc}}/s_d$	0.0	1.0
$\eta$	layer intermixing	0.0	1.0
$\sigma_r$ / nm	r.m.s. roughness	0.0	0.5
$\rho_{\text{Sc}}$	Sc density w.r.t. bulk density	0.5	1.0
$\rho_{\text{Cr}}$	Cr density w.r.t. bulk density	0.5	1.0

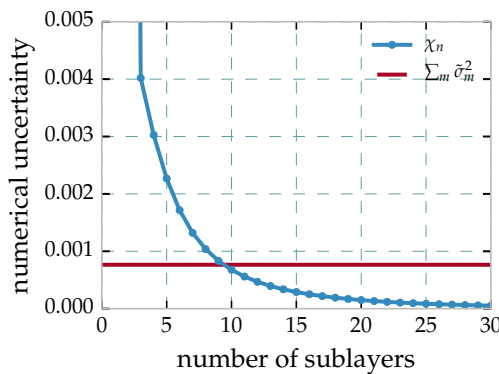
account for diffusely scattered light, which is missing in the measured specularly reflected radiation but can not be attributed to contrast loss due to interdiffusion. The parameter  $\Gamma_{\text{Sc}}$  indicates the portion of the Sc layer thickness with respect to the full period thickness  $D$ , which together uniquely define the thickness  $d_{\text{Cr}}$ ;  $\Gamma_s$  describes the asymmetry of the widths of the interdiffusion zones at the Cr on Sc and Sc on Cr interfaces and is intrinsically limited to the interval  $\Gamma_s \in [0, 1]$ . Note that  $s_{\text{Sc}}$  and  $s_{\text{Cr}}$  are half periods of the sinus functions used to describe the interface profiles. Therefore the condition  $s_{\text{Sc}} + s_{\text{Cr}} \leq D$  holds.

The discretization of the smooth interface profile in the interdiffusion zones introduces an additional numerical uncertainty through the number of discretization points  $n$  required to reflect the physical situation of a smooth transition. To assert a lower limit for this number, we have evaluated the mean error introduced by coarse sampling. The most accurate experiment of the analysis within this chapter is given by the EUV reflectivity curve, which serves as a reference for this assertion through the sum of the squared uncertainty of each data point in Fig. 1.16a,  $\sum_m \tilde{\sigma}_m$ .

The numerical error of the model depending on the interface sampling through gradual sublayers was evaluated by comparing the sum of squares

$$\chi_n = \sum_m (I_m^{n=100} - I_m^n)^2 \quad (1.8)$$

of the difference theoretical EUV curves with increasing numbers of gradual interfaces and an “ideal” smooth transition represented by 100 sublayers. The model parameters used for this analysis were obtained through a PSO optimization of the model with respect to the EUV reflectivity curve. As illustrated in Fig. 1.20, the experimental


**Figure 1.20** | Numerical uncertainty

uncertainty dominates at the lower limit of  $n = 10$  sublayers for the interface zone. For the analysis in this chapter, and due to reasons of numerical effort required to calculate the electromagnetic field for all measurements discussed here, we use  $n = 15$  sublayers for all calculations. At that value, the experimental uncertainty is clearly dominant and only a marginal additional uncertainty is acquired due to insufficient sampling.

As a verification of the applicability of the model to the problem of accurately representing a physical situation that could describe the EUV and XRR data shown in Fig. 1.16 above, we have applied the combined analysis technique for the two data sets described in Sec. 1.2.2 to the improved gradual model. The particle swarm optimization approach applied to obtain a global solution for the model parameters by minimizing the functional defined in Eq. (1.6). The results found for the binary model (cf. Fig. 1.18) and the gradual model are shown in direct comparison with each other in Fig. 1.21. The EUV reflectivity

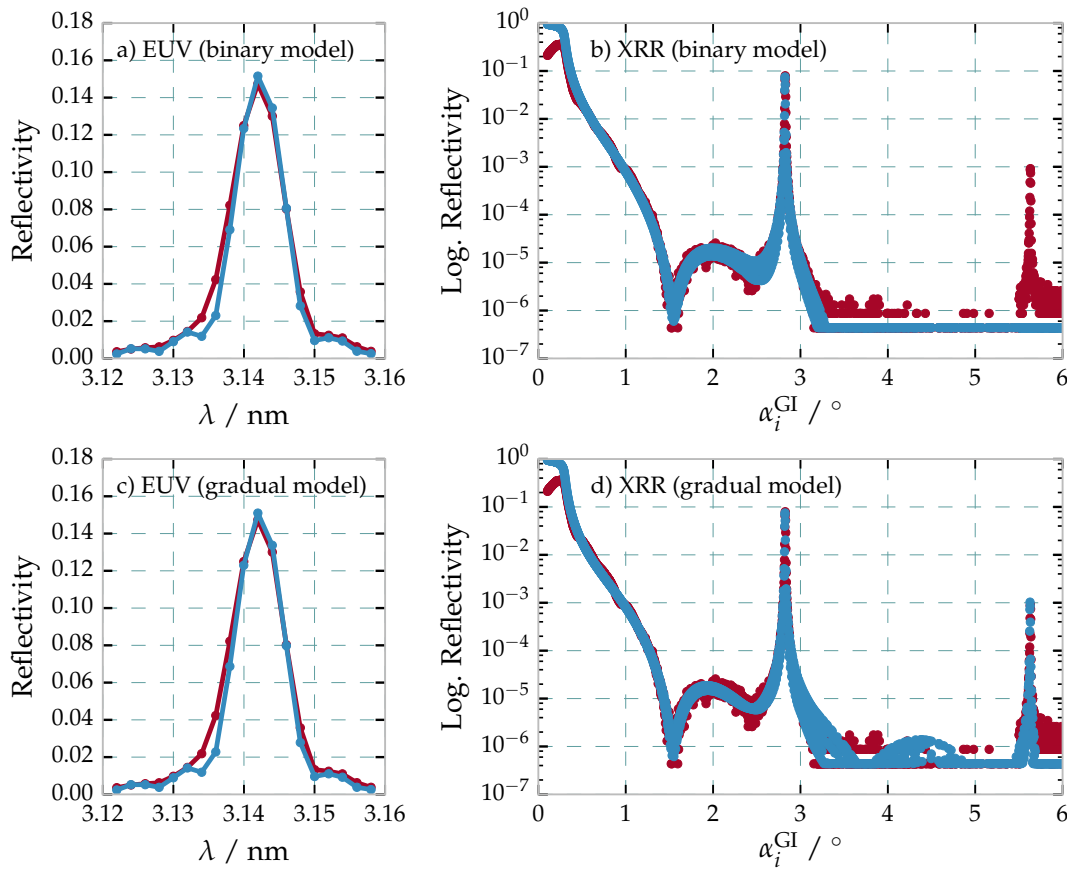


**Figure 1.21** | Comparison of the reconstructions of both models for the EUV and XRR data. a) Measured EUV reflectivity curve for and near-normal angle of incidence of  $\alpha_i = 1.5^\circ$  together with calculated curve of the PSO-based binary model reconstruction. b) Measured and calculated XRR curves for the same sample and model parameters at grazing angles of incidence using radiation at the Cu- $K_\alpha$  wavelength. A clear mismatch of the theoretical curve and the measured data can be observed for the second Bragg peak between  $\alpha_i^{\text{GI}} = 5.0^\circ$  and  $\alpha_i^{\text{GI}} = 6.0^\circ$ . c) Measured EUV reflectivity curve for and near-normal angle of incidence of  $\alpha_i = 1.5^\circ$  together with calculated curve of the PSO-based gradual model reconstruction. d) Measured and calculated XRR curves for the same sample and model parameters at grazing angles of incidence using radiation at the Cu- $K_\alpha$  wavelength.

curves show visually indistinguishable fits for both, the binary model as already found above and also the gradual model in Fig. 1.21a and Fig. 1.21c. For the binary model, we have seen the distinct mismatch with the second order Bragg peak, which is shown once

again in Fig. 1.21b. For the gradual interface model, we see a significant improvement of the optimized result with perfectly match in both Bragg peaks of the XRR curve in Fig. 1.21d while also maintaining an excellent agreement with the EUV curve.

Based on the example of a combined analysis of EUV and XRR data in this section, the gradual interface model clearly provides a more accurate representation of the physical reality in the sample than the binary approach by offering a reconstruction satisfying both data sets. At the same time, the results show that a verification of the model only becomes possible by adding complementary information. In case of the example above, that information is provided through the appearance of a second Bragg peak in the XRR curve. Thereby, the limiting case of the binary model, which is still possible for the new gradual model, can be excluded with certainty through the comparison shown in Fig. 1.21. The main difference of both models is the local gradual change of the index of refraction, which attributes for the fact that both materials can intermix. More importantly, both materials can intermix differently with respect to the specific interface, i.e. the situation where Cr is deposited on top of Sc or vice versa. A key element of obtaining a reconstruction of that particular model is thus the application of techniques, which can deliver information on the spacial distribution of the materials within one period.

At that point, it should be noted that other distortions of a perfect layer system can be imagined, which are not covered by a strictly periodic model as the one introduced above. Those include drifts of the period thickness  $D$  across the stack or other systematic aperiodicities. In that case, however, a broadening of the peak or a distortion of the peaks symmetry, most prominently in the EUV curve, would be observed, which is not the case. Although situations may occur, where the aperiodicities could lead to effects compensated by tuning the parameters of the gradual interface model, this assumption would assume a more complex situation than the simple assumption of periodicity and is thus implausible.

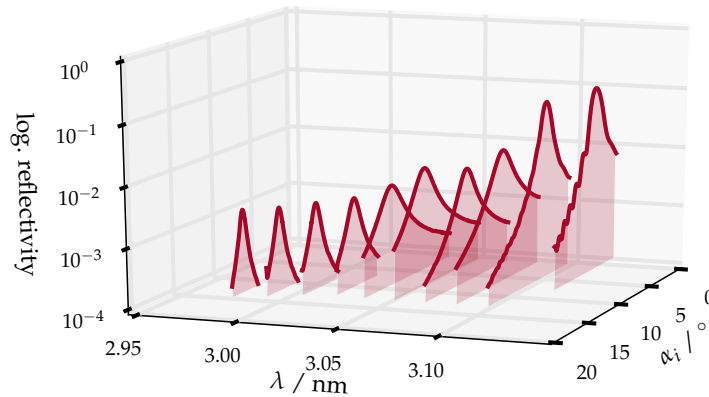
### 1.3.3 Addition of Complementary Experimental Methods

Due to the increased complexity of the model, the question arises how accurately any parameter of the model can be determined and whether correlations exist and can be resolved (cf. Fig. 1.11 as an example for correlated model parameters in case of Mo/Si multilayer systems) based on the available data and whether further analytical measurements can improve the result as this was clearly the result for the EUV and XRR experiments shown above. For the particular case of the gradual interface model for periodic multilayer systems with sub-nanometer layer thicknesses, in total four experiments were conducted with the goal to find a unequivocal reconstruction including low enough confidence intervals.

### Resonant EUV Reflectivity

As seen for the four layer system discussed in Sec. 1.1, confidence intervals for the individual layer thicknesses in the range below 1 nm could not be obtained by exclusively analyzing the EUV curve. Similarly, the combined analysis of EUV and XRR experiments in Sec. 1.2.2 did improve the result but still shows fairly large confidence intervals concerning the small total layer thickness in the Cr/Sc systems. For the particular system discussed here with possibly strong interdiffusion, a technique is required that yields the total amount of Sc and equivalently Cr within a single period. For that purpose, resonant reflectivity experiments in the EUV spectral range are promising. The knowledge of the optical constants are a necessary requirement for deducing quantitative information from that kind of experiment. In case of Sc, those were measured precisely for the Sc L<sub>3</sub> and L<sub>2</sub> absorption edges at approximately  $\lambda_{\text{Sc-L}} \approx 3.1$  nm and below by Aquila et al. [2]. The real and imaginary parts obtained from that experiments are shown together with the respective optical constants of Cr in Fig. ?? of Sec. ?? in Ch. ?. To exploit the information contained in the optical constants of Sc, angular resolved reflectivity curves across the first Bragg peak were recorded at several wavelengths across the Sc L-edge. As the Cr dispersion is changing only marginally and smoothly across that wavelength range, any change of contrast and absorption can be attributed to the Sc in the multilayer. The corresponding measurements are shown in Fig. 1.22. Each reflectivity curve was

**Figure 1.22** | REUV



recorded within the interval from  $\alpha_i = 2.5^\circ$  to  $\alpha_i = 19.0^\circ$ , depending on the selected wavelength. The wavelength range was chosen between  $\lambda = 2.986$  nm and  $\lambda = 3.128$  nm including the Sc L<sub>2</sub> and L<sub>3</sub> edges. The resulting data is analyzed in analogy to the EUV reflectivity curves in Sec. 1.3.2 by applying the matrix algorithm on basis of the gradual layer model and the optical constants by Aquila et al. [2]. The experimental uncertainties taken into account for the resonant extreme ultraviolet reflectivity (REUV) experiment were estimated on basis of the multilayer inhomogeneity deducted as described for the EUV experiment in Sec. 1.3.1. The details of the reconstruction based on this dataset are shown below in this section.

## Grazing Incidence X-ray Fluorescence

In addition to the reconstruction of the Sc content via the REUV experiment, spacial resolved measurements are necessary to deduct the interface profile in the gradual layer model. As discussed in Sec. 1.3.2, asymmetric interface regions provide a possibility to observe a second Bragg peak in the XRR measurement, even though both layers in the period have equal nominal thickness. To obtain information on that spacial distribution of both materials within a period, XRF experiments exploiting the formation of a standing wave when scanning across the first Bragg peak were performed. The details of the method and how spacial sensitivity can be obtained are described in detail in Ch. ??, Sec. ??.

The sample was measured exciting the Sc and Cr K-lines, which show the highest fluorescence yield for the core shell transitions. The K-edges for both materials are at energies of  $E_{\text{Sc-K}} = 4492 \text{ eV}$  and  $E_{\text{Cr-K}} = 5989 \text{ eV}$  [9]. The experiment was therefore conducted at the four crystal monochromator (FCM) beamline in grazing incidence geometry at photon energies of  $E_{\text{ph}} = 5500 \text{ eV}$  and  $E_{\text{ph}} = 6250 \text{ eV}$ , well above the respective edges as described in Ch. ??, Sec. ??. Depending on which energy was used, the Bragg peak is found at grazing angles of incidence of  $\alpha_i^{\text{GI}} \approx 4.12^\circ$  and  $\alpha_i^{\text{GI}} \approx 3.62^\circ$ , respectively. The measured relative fluorescence yield in the vicinity of the first Bragg peak is shown in Fig. 1.23 for both photon energies and materials. Since the photon energy

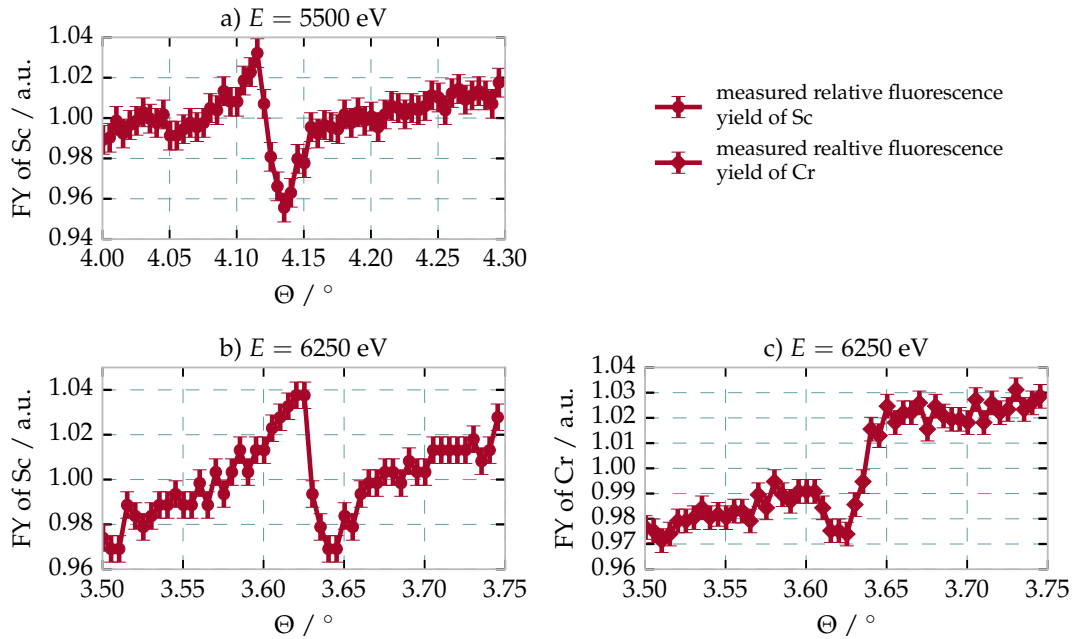


**Figure 1.23** | XRF

of  $E_{\text{ph}} = 5500 \text{ eV}$  is below the K-edge of Cr, only data for the Sc K-fluorescence exists. In the second case, fluorescence from both materials was detected. The measurement uncertainties were estimated from the distribution of the data for regions away from the Bragg resonance.

The fluorescence curves for Cr and Sc show distinctly different behavior, of the expected s-curve-shape (cf. Fig. ??). For the analysis, the result at photon energies of  $E_{\text{ph}} = 5500 \text{ eV}$  (Fig. 1.23a) was not taken into account, as the information is redundant to the result at  $E_{\text{ph}} = 6250 \text{ eV}$  (Fig. 1.23b). As mentioned above, the theoretical description on how the

relative fluorescence is calculated based on the gradual model is elaborated on in detail in Ch. ??, Sec. ??.

### 1.3.4 Reconstruction and Maximum Likelihood Evaluation

With the two additional measurements described above, the total of four data sets (EUV, XRR, REUV and XRF) are available for the Cr/Sc multilayer sample to reconstruct the parameters of the gradual interface model. The full dataset is compiled in Fig. 1.24.

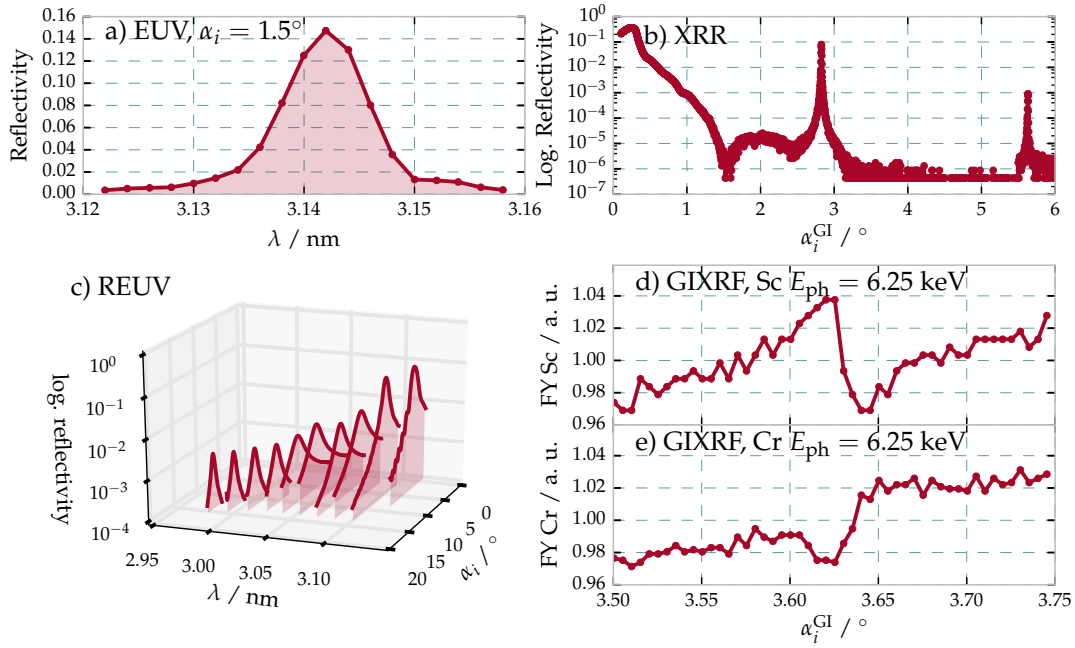


**Figure 1.24** | All relevant data

As in the combined analysis conducted for the Mo/Si/C systems in Sec. 1.2.2, we define the minimization functional for the combined analysis of all the datasets as

$$\chi^2 = \tilde{\chi}_{\text{EUV}}^2 + \tilde{\chi}_{\text{XRR}}^2 + \tilde{\chi}_{\text{REUV}}^2 + \tilde{\chi}_{\text{GIXRF(Sc)}}^2 + \tilde{\chi}_{\text{GIXRF(Cr)}}^2, \quad (1.9)$$

where each of the reduced functionals is defined as

$$\tilde{\chi}^2 = \frac{1}{M - P} \left[ \sum_m \frac{(I_m^{\text{model}} - I_m^{\text{meas}})^2}{\tilde{\sigma}_m^2} \right], \quad (1.10)$$

with  $M$  being the number of measurement points in each experiment and  $P$  the number of parameters for the model. Statistical and systematic uncertainties for each data point are included in  $\tilde{\sigma}_m$ . The definition of Eq. (1.9) ensures that all experiments are weighted equally considering their respective uncertainties. This functional corresponds to the combined  $\chi^2$  functional defined in (1.6), augmented by the additional measurements conducted here.

Firstly, similar as for the other two sample systems treated in this chapter, the parameters of the model, here the gradual interface model with the parameters and their limits listed in table 1.9, were obtained using the PSO method to find a solution reproducing the experimental results. Secondly, following the maximum likelihood approach employing

the MCMC method as detailed in Sec. 1.1.2, starting from this the uniqueness and confidence intervals for each parameter were obtained. The PSO result was further refined by taking the 50% percentile of the resulting likelihood distribution for each parameter.

Through the minimization of the combined  $\chi^2$  functional in Eq. (1.9) via the PSO method, the best model parameters were obtained. It should be noted here, that in case of the XRR curve, the analyzed data set was restricted to the two visible Bragg peaks which contain the information on the periodic part of the layer system. The data in between those does reflect the top surface layer thicknesses and was therefore analyzed separately to obtain the capping layer thicknesses after the optimization of the periodic part. The results for the capping layer thicknesses listed in table 1.10 was consequently used throughout the theoretical analysis for all experiments described here.

Parameter	XRR (areas in between the peaks)
$d_{\text{C (cap)}} / \text{nm}$	0.709
$d_{\text{CrO (cap)}} / \text{nm}$	0.913
$d_{\text{Cr (cap)}} / \text{nm}$	2.495
$\rho_{\text{C (cap)}}$	0.527
$\rho_{\text{CrO (cap)}}$	0.548
$\rho_{\text{Cr (cap)}}$	0.791

**Table 1.10** | Optimized model parameters obtained by PSO analysis

## Confidence Intervals and Evaluation of the Experimental Methods

As discussed numerously throughout this chapter, the single optimization based on an PSO result ideally delivers a global minimum of the respective optimization functional. However, no information is obtained about the uniqueness and accuracy of the solution or correlation of parameters causing ambiguity of the results. Consequently, in addition to fitting the data with a particle swarm optimizer, each result was verified based on the MCMC method described above to evaluate the confidence intervals for each parameter. To assess the performance of each of the experimental methods individually, the two step process, i.e. the PSO fitting procedure followed by the MCMC sampling, was conducted for each standalone experiment as well as for the combined optimization problem stated in Eq. (1.9).

The results are compiled in Table 1.11. The confidence intervals were calculated by evaluating the probability distribution as a result of the MCMC procedure for each parameter around its PSO fit results. The confidence intervals given here represent percentiles of the number of samples found in the interval defined by the upper and lower bounds used for the PSO procedure for each parameter. In the case of a centered Gaussian distribution, percentiles of 2.3% and 97.8% of the integrated number of samples forming the distribution, mark the interval of four times the standard deviation, i.e.  $\pm 2\sigma$  in statistical terms. Due to potential asymmetries in the actual distributions found by the MCMC method, explicit upper and lower bounds of the confidence intervals are given in table 1.11 based on these percentiles. The best model value is based on the PSO fit result and is refined by the MCMC sampling by calculating the mean value, i.e. the 50% percentile, of the distribution of samples following the MCMC procedure.

Before discussing the achieved reconstruction and the corresponding confidence intervals of each of the methods in detail, we shall view the theoretical curves calculated from the best model of the combined analysis. The curves are shown in direct compar-

## CHARACTERIZATION OF THE MULTILAYER STRUCTURE FOR DIFFERENT SYSTEMS

**Table 1.11** | Optimized model parameters with confidence intervals derived from MCMC validation for each individual experiment and the combined analysis

Parameter	Combined	EUV	XRR	REUV	GIXRF
$D$ / nm	$1.5737^{+0.0008}_{-0.0010}$	$1.5749^{+0.0014}_{-0.0022}$	$1.5726^{+0.0035}_{-0.0042}$	$1.5728^{+0.0016}_{-0.0019}$	$1.5741^{+0.0021}_{-0.0024}$
$\Gamma_{Sc}$	$0.48^{+0.04}_{-0.04}$	$0.35^{+0.14}_{-0.11}$	$0.42^{+0.35}_{-0.26}$	$0.52^{+0.09}_{-0.07}$	$0.49^{+0.09}_{-0.10}$
$s_d$ / nm	$1.34^{+0.18}_{-0.26}$	$0.72^{+0.67}_{-0.66}$	$0.60^{+0.78}_{-0.57}$	$0.89^{+0.59}_{-0.83}$	$1.27^{+0.24}_{-0.38}$
$\Gamma_{\sigma}$	$0.16^{+0.51}_{-0.16}$	$0.29^{+0.64}_{-0.28}$	$0.40^{+0.57}_{-0.39}$	$0.33^{+0.61}_{-0.32}$	$0.39^{+0.57}_{-0.37}$
$\eta$	$0.56^{+0.06}_{-0.16}$	$0.44^{+0.16}_{-0.30}$	$0.38^{+0.33}_{-0.36}$	$0.52^{+0.14}_{-0.37}$	$0.37^{+0.25}_{-0.34}$
$\sigma_r$ / nm	$0.11^{+0.11}_{-0.10}$	$0.17^{+0.12}_{-0.15}$	$0.13^{+0.14}_{-0.12}$	$0.17^{+0.16}_{-0.16}$	$0.27^{+0.20}_{-0.25}$
$\rho_{Sc}$	$0.94^{+0.05}_{-0.12}$	$0.84^{+0.15}_{-0.32}$	$0.78^{+0.21}_{-0.27}$	$0.94^{+0.06}_{-0.14}$	$0.83^{+0.17}_{-0.30}$
$\rho_{Cr}$	$0.98^{+0.02}_{-0.08}$	$0.96^{+0.04}_{-0.13}$	$0.83^{+0.16}_{-0.27}$	$0.90^{+0.09}_{-0.21}$	$0.86^{+0.14}_{-0.28}$

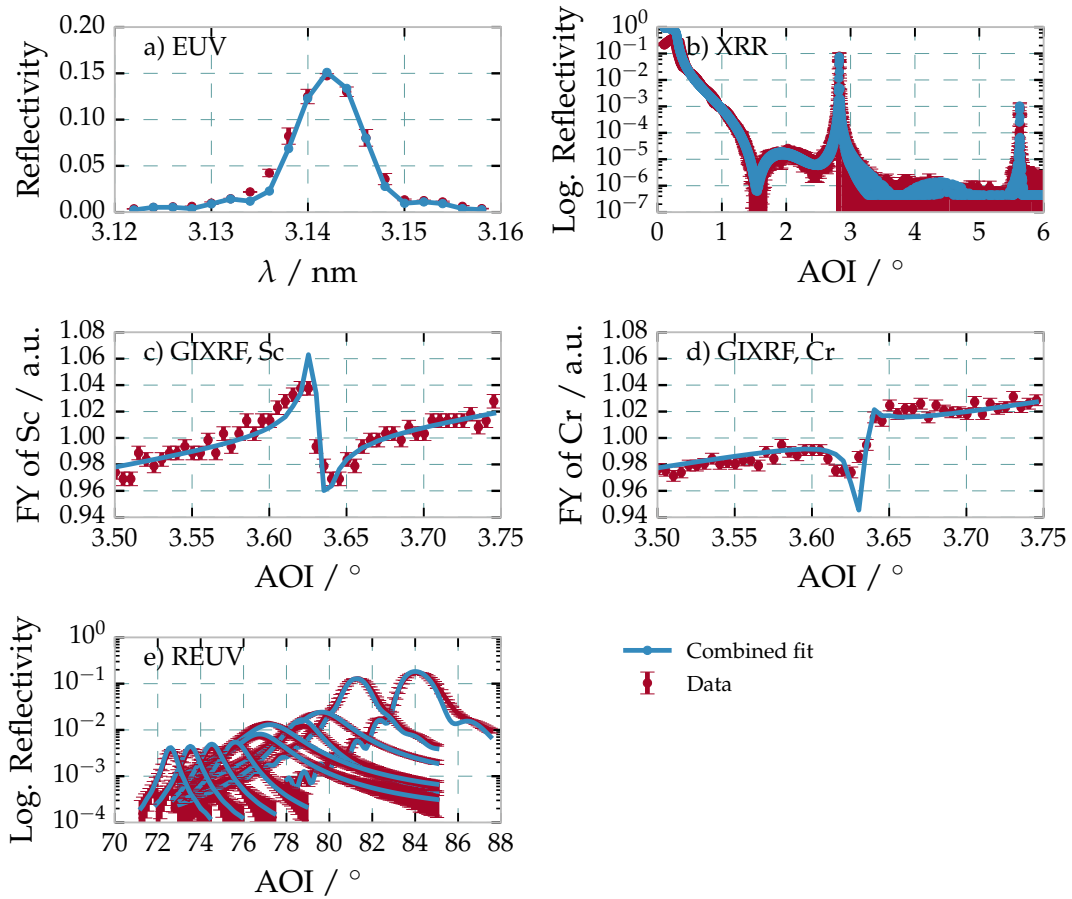


**Figure 1.25** | Measured and calculated reflectance and intensity curves for the optimized parameters with the combined analysis of all experiments as listed in Table ??.



ison with the data from Fig. 1.24 including the respective experimental uncertainties in Fig. 1.25. Clearly, the data and the solution found in the optimization procedure show excellent agreement indicating that the gradual interface model indeed provides a very good representation of physical reality with respect to the experiments conducted here. Nevertheless, differences can be observed. The reason lies in the fact that the model is potentially still too ideal. Small variations during the deposition process, for example, could lead to imperfections, which are not described in a strictly periodic model. However, including these by explicitly breaking the periodicity would again lead to an ill-defined model with a vastly increased number of parameters and is thus not practical. Another reason is the deviation in the homogeneity of the sample, e.g. a varying period across the sample, which cause mismatches if the measurement position varies slightly between the different experimental setups. The latter effects were considered in the uncertainties of the individual measurements by measuring the EUV reflectivity at positions  $\pm 2$  mm from the center position and fitting the model. The result was a  $\Delta D = 2$  pm shift in the period over 4 mm across the sample.

### Parameter correlations in the combined analysis

With the optimized model parameters listed in table 1.11 and shown in Fig. 1.25 for the combined analysis, a model reconstruction could be obtained explaining the data for each of the experiments. The MCMC sampling of the likelihood functional based on the  $\chi^2$  definition in Eq. (1.9) yields the corresponding confidence intervals for all parameters and experiments given through the upper and lower bound as described above. Here, we shall illustrate and discuss in detail the resulting likelihood distributions obtained from the combined analysis, as they show that correlations of the parameters could be resolved and only persist for a single important case. For that, Fig. 1.26 shows the full matrix of two- and one-dimensional likelihood distribution projections marginalizing over all other parameters. The details of how this figure is to be interpreted are described in detail above in Sec. 1.1.2 for the example of Mo and Si layer thicknesses obtained through fitting EUV reflectivity data. Here, all possible gradual interface model parameter combinations are shown as two dimensional histograms together with the one-dimensional projection at the diagonal of the plot matrix. The solid blue line represents the values of the optimized model after both, the PSO and refining through the MCMC method. They correspond to the values listed in table 1.11 for the combined analysis column.

Generally, most of the parameter combinations do not show distinct correlations but approach the shape of a two-dimensional Gaussian distribution, which would be expected for a unique solution with corresponding uncertainty. It should be noted that in some cases, the distribution is truncated by parameter limits, which follow from physical or mathematical restrictions on the parameters as discussed in Sec. 1.3.2, such as for the densities  $\rho_{\text{Sc}}$  and  $\rho_{\text{Cr}}$  as well as for the interface region ratio  $\Gamma_{\sigma}$ . In addition, the latter parameter shows a bimodal distribution for all two-dimensional histograms with clear emphasis on the lower value. That is a particularly interesting result of the combined analysis as it clearly demonstrates that only strongly asymmetric interface regions are minimizing the  $\chi^2$  functional and it may thus be concluded that this corresponds to the physical reality in the sample.

Finally, the parameter set of the r.m.s. roughness  $\sigma_r$  and the interdiffusion parameter  $\eta$  show a “banana shaped” correlation significantly broadening the confidence intervals for both parameters. Fig. 1.27 shows a magnification of that particular histogram to

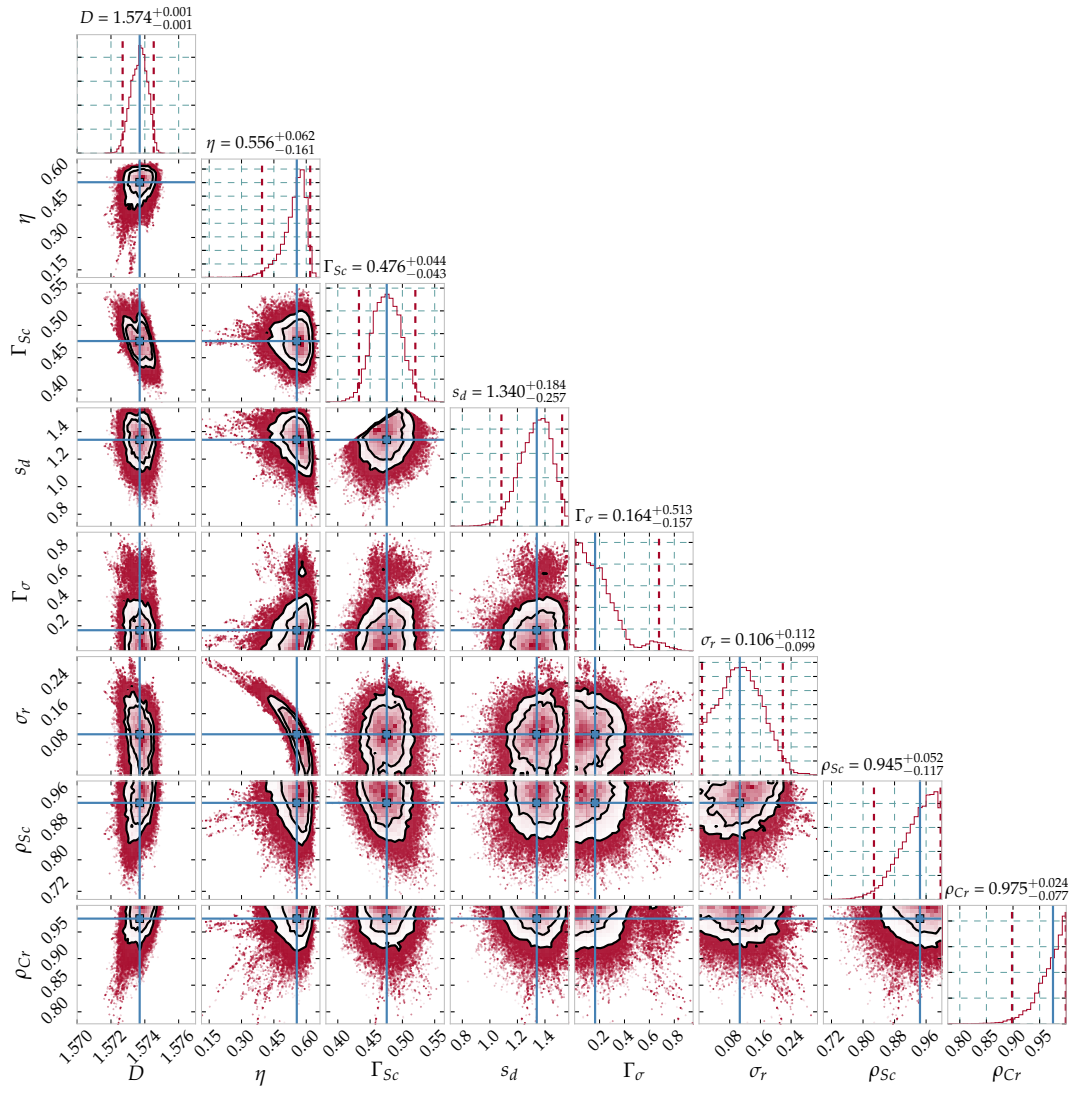
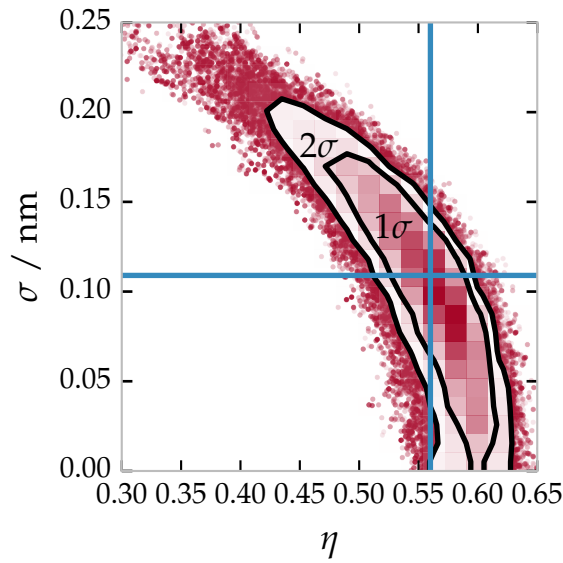


Figure 1.26 | Cornerplot

better illustrate this property. The broad spectrum of values covered by the distribution



**Figure 1.27** | CrSc eta rho correlation

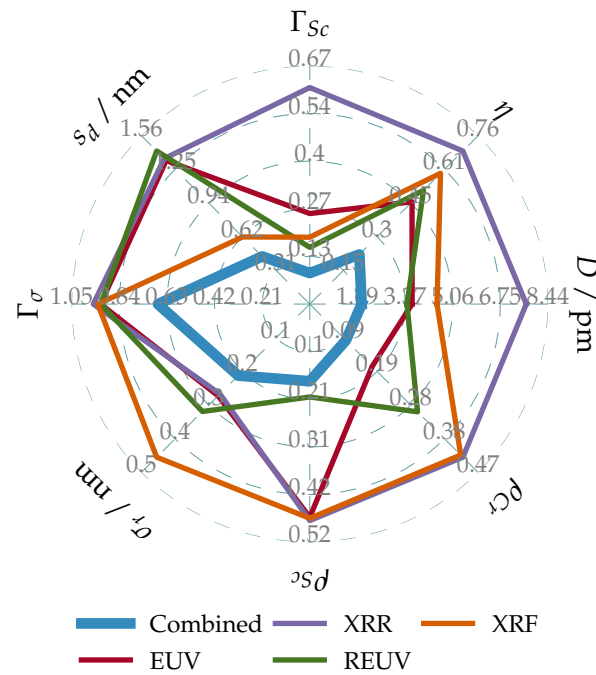
in both parameters hints at a indistinguishability of those two model parameters, and consequently physical properties of the sample, based on the analyzed data. In fact, this conclusion can easily be understood as none of the applied experimental methods can separate the effect of roughness and interdiffusion. For better understanding this, we shall consider the relatively large beam footprint, with the smallest one of all experiments covering an area of approximately 1 mm by 1 mm, in comparison to the roughness dimensions and frequencies expected in the order of nanometers. Thereby, any reflected radiation or fluorescence radiation excited within the multilayer always represents an average of the rough interface morphology. That, however, can not be distinguished from a homogeneous layer with gradual interdiffusion along the surface normal of the sample. The solution to this problem of distinction is the analysis of diffuse scattering from the sample in addition to the combined analysis, which is the topic of the Ch. ?? of this thesis.

### Confidence intervals depending on the employed method

The confidence intervals of each experimental method differ significantly as table 1.11 shows. The reason behind this is the different sensitivity of the methods to the specific physical properties described by the respective model parameter. To better illustrate the information compiled in the table above, for each method and each parameter the total confidence interval is shown in Fig. 1.28 in a radial plot. The total confidence interval is defined as the difference of the upper and lower values as listed in table 1.11 for each experiment and parameter. The plot shows the four relevant experiments and the combined analysis results. Any value closer to the origin of the radial plot indicates a smaller confidence interval and thus a better accuracy of the solution found for the respective parameter.

It is worth noting that the confidence interval for the combined analysis is significantly smaller compared to the individual experiments for all parameters and therefore yields the best result. This is especially true for the parameter  $\Gamma_\sigma$  describing the asymmetry of the interdiffusion layers. Within each of the individual experiments this parameter has a large uncertainty and can not be determined, whereas the combined analysis delivers a

**Figure 1.28** | Visual representation of the total confidence intervals for each of the parameters with respect to each of the individual experiments as well as the combined analysis.



significant result of a clearly asymmetric interdiffusion layer thickness. In combination with the observations made above for the respective histograms in Fig. 1.26, we can conclude that this asymmetry is indeed a significant result and that the remaining fairly large confidence interval mainly results from the fact of having a bimodal distribution as the dotted lines in the respective histogram Fig. 1.26 prove. A possible explanation for this asymmetry is the deposition process through magnetron sputtering. The elements Cr and Sc have different mass and thus different momentum when deposited onto each other. A similar effect is known from the deposition of Mo/Si multilayer systems, where the heavier Mo shows higher penetration into the Si layer than vice versa [26]. In the case of Cr/Sc multilayers, the Cr is heavier and thus has higher momentum leading to a broader interdiffusion layer, which is indeed also the interface region found to be the broadest by the analysis conducted here.

The final result of this analysis of Cr/Sc multilayer systems with sub-nanometer layer thicknesses is shown in Fig. 1.29 by the depth dependence of the index of refraction in direct comparison with the initial binary model. As mentioned before, the most remarkable result of the combined analysis is the strong asymmetry of the interdiffusion layers. This can only be shown by the combination of all analytical experiments conducted here. In addition, the comparison shows that at no point within the periodic multilayer stack pure Sc or pure Cr layers are observed, but always a mixture of both. In the context of answering the question of poor reflectivity with respect to the theoretical possible maximum, this shows that interdiffusion may be the main reason. The loss of contrast with respect to the binary model indicated, causes the diminished reflectivity. We should note, however, that due to the correlation between roughness and interdiffusion this result is still to be verified by the aforementioned analysis of diffuse scattering. This is the topic of chapter ??.

The experiments, methods and findings of this section are part of the publication A. Haase, S. Bajt, P. Höncke, V. Soltwisch and F. Scholze: 'Multiparameter characterization of subnanometre Cr/Sc multilayers based on complementary measurements'.

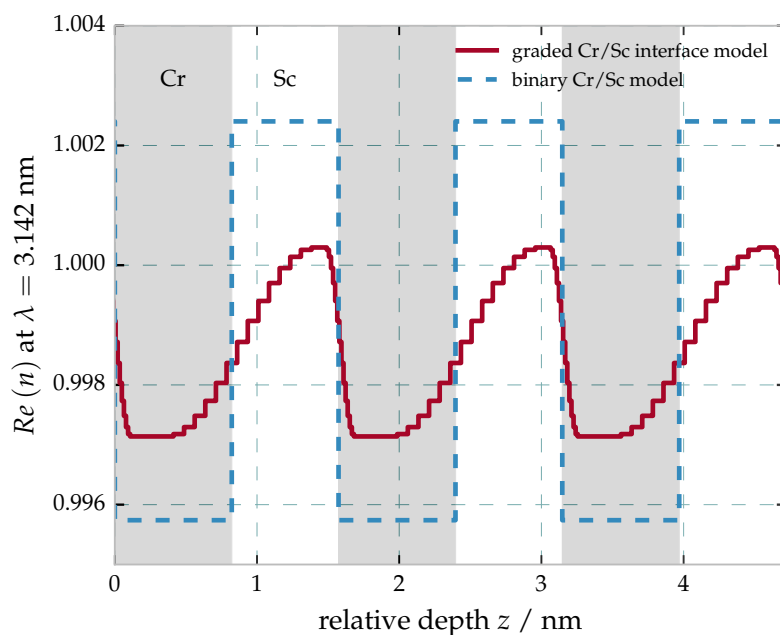


**Figure 1.29** | Real part of the index of refraction  $n$  based on the results of the optimized parameters listed in Table ?? for the combined analysis for a selected wavelength. The gradual interface model is shown in direct comparison to the binary model optimized for the EUV reflectance curve over three full periods. The resulting strong asymmetry in the width of the interface regions is clearly visible (see text). The gray and white shaded areas indicate the Cr and Sc layers, respectively, for the binary model.

en. In: *Journal of Applied Crystallography* **49.6** (Dec. 2016), pp. 2161–2171. DOI: 10.1107/S1600576716015776



# References

- [1] M. Abramowitz and I. A. Stegun: *Handbook of Mathematical Functions: With Formulas, Graphs, and Mathematical Tables*. en. Courier Corporation, 1964.
- [2] A. L. Aquila, F. Salmassi, E. M. Gullikson, F. Eriksson and J. Birch: ‘Measurements of the optical constants of scandium in the 50-1300eV range’. In: vol. 5538. 2004, pp. 64–71. DOI: 10.1117/12.563615.
- [3] S. Bajt, D. G. Stearns and P. A. Kearney: ‘Investigation of the amorphous-to-crystalline transition in Mo/Si multilayers’. In: *Journal of Applied Physics* **90.2** (2001), pp. 1017–1025. DOI: <http://dx.doi.org/10.1063/1.1381559>.
- [4] M. Bayes and M. Price: ‘An Essay towards Solving a Problem in the Doctrine of Chances. By the Late Rev. Mr. Bayes, F. R. S. Communicated by Mr. Price, in a Letter to John Canton, A. M. F. R. S.’ en. In: *Philosophical Transactions* **53** (1763), pp. 370–418. DOI: 10.1098/rstl.1763.0053.
- [5] R. T. Birge: ‘The Calculation of Errors by the Method of Least Squares’. In: *Physical Review* **40.2** (1932), pp. 207–227. DOI: 10.1103/PhysRev.40.207.
- [6] S. Braun, H. Mai, M. Moss, R. Scholz and A. Leson: ‘Mo/Si Multilayers with Different Barrier Layers for Applications as Extreme Ultraviolet Mirrors’. en. In: *Japanese Journal of Applied Physics* **41.6S** (2002), p. 4074. DOI: 10.1143/JJAP.41.4074.
- [7] A. Carlisle and G. Dozier: ‘An off-the-shelf PSO’. In: *Proceedings of The Workshop On particle Swarm Optimization, Indianapolis, USA*. 2001.
- [8] D. R. Cox and D. V. Hinkley: *Theoretical Statistics*. en. CRC Press, 1979.
- [9] W. T. Elam, B. D. Ravel and J. R. Sieber: ‘A new atomic database for X-ray spectroscopic calculations’. In: *Radiation Physics and Chemistry* **63.2** (2002), pp. 121–128. DOI: 10.1016/S0969-806X(01)00227-4.
- [10] D. Foreman-Mackey, D. W. Hogg, D. Lang and J. Goodman: ‘emcee: The MCMC Hammer’. In: *Publications of the Astronomical Society of the Pacific* **125.925** (2013). arXiv: 1202.3665, pp. 306–312. DOI: 10.1086/670067.
- [11] C. F. Gauss: *Theoria motus corporum coelestium in sectionibus conicis solem ambientium*. en. 1809.
- [12] J. Goodman and J. Weare: ‘Ensemble samplers with affine invariance’. en. In: *Communications in Applied Mathematics and Computational Science* **5.1** (2010), pp. 65–80. DOI: 10.2140/camcos.2010.5.65.

## References

- [13] A. Haase, S. Bajt, P. Hönicke, V. Soltwisch and F. Scholze: 'Multiparameter characterization of subnanometre Cr/Sc multilayers based on complementary measurements'. en. In: *Journal of Applied Crystallography* **49.6** (2016), pp. 2161–2171. DOI: 10.1107/S1600576716015776.
- [14] A. Haase, V. Soltwisch, S. Braun, C. Laubis and F. Scholze: 'Interface Morphology of Mo/Si Multilayer Systems with Varying Mo Layer Thickness Studied by EUV Diffuse Scattering'. In: *Optics Express* (2017).
- [15] A. Haase, V. Soltwisch, C. Laubis and F. Scholze: 'Role of dynamic effects in the characterization of multilayers by means of power spectral density'. In: *Appl. Opt.* **53.14** (2014), pp. 3019–3027. DOI: 10.1364/AO.53.003019.
- [16] A. Haase, V. Soltwisch, F. Scholze and S. Braun: 'Characterization of Mo/Si mirror interface roughness for different Mo layer thickness using resonant diffuse EUV scattering'. In: *Proc. SPIE*. Vol. 9628. 2015, pp. 962804–962804–7. DOI: 10.1117/12.2191265.
- [17] B. L. Henke, E. M. Gullikson and J. C. Davis: 'X-Ray Interactions: Photoabsorption, Scattering, Transmission, and Reflection at  $E = 50\text{--}30,000$  eV,  $Z = 1\text{--}92$ '. In: *Atomic Data and Nuclear Data Tables* **54.2** (1993), pp. 181–342. DOI: <http://dx.doi.org/10.1006/adnd.1993.1013>.
- [18] M. P. Hobson and J. E. Baldwin: 'Markov-chain Monte Carlo approach to the design of multilayer thin-film optical coatings'. EN. In: *Applied Optics* **43.13** (2004), pp. 2651–2660. DOI: 10.1364/AO.43.002651.
- [19] J. Kennedy: 'Particle Swarm Optimization'. en. In: *Encyclopedia of Machine Learning*. Ed. by C. Sammut and G. I. Webb. DOI: 10.1007/978-0-387-30164-8\_630. Springer US, 2011, pp. 760–766.
- [20] H. Kiessig: 'Interferenz von Röntgenstrahlen an dünnen Schichten'. In: *Annalen der Physik* **402.7** (1931), pp. 769–788. DOI: 10.1002/andp.19314020702.
- [21] A.-M. Legendre: *Nouvelles méthodes pour la détermination des orbites des comètes*. fr. F. Didot, 1805.
- [22] K. Levenberg: 'A method for the solution of certain non-linear problems in least square'. In: *Quarterly of Applied Mathematics* (1944).
- [23] Y. Lim, T. Westerwalbesloh, A. Aschentrup, O. Wehmeyer, G. Haindl, U. Kleineberg and U. Heinzmann: 'Fabrication and characterization of EUV multilayer mirrors optimized for small spectral reflection bandwidth'. In: *Applied Physics A* **72.1** (2001), pp. 121–124. DOI: 10.1007/s003390000723.
- [24] D. W. Marquardt: 'An algorithm for least-squares estimation of nonlinear parameters'. In: *Journal of the society for Industrial and Applied Mathematics* **11.2** (1963), pp. 431–441.
- [25] J. S. Milton and J. C. Arnold: *Introduction to Probability and Statistics: Principles and Applications for Engineering and the Computing Sciences*. 4th. New York, NY, USA: McGraw-Hill, Inc., 2002.
- [26] A. K. Petford-Long, M. B. Stearns, C.-H. Chang, S. R. Nutt, D. G. Stearns, N. M. Ceglio and A. M. Hawryluk: 'High-resolution electron microscopy study of x-ray multilayer structures'. In: *Journal of Applied Physics* **61.4** (1987), pp. 1422–1428. DOI: <http://dx.doi.org/10.1063/1.338122>.



- [27] M. Prasciolu, A. Haase, F. Scholze, H. N. Chapman and S. Bajt: 'Extended asymmetric-cut multilayer X-ray gratings'. EN. In: *Optics Express* **23.12** (2015), pp. 15195–15204. DOI: 10.1364/OE.23.015195.
- [28] M. Prasciolu, A. F. G. Leontowich, K. R. Beyerlein and S. Bajt: 'Thermal stability studies of short period Sc/Cr and Sc/B<sub>4</sub>C/Cr multilayers'. In: *Appl. Opt.* **53.10** (2014), pp. 2126–2135. DOI: 10.1364/AO.53.002126.
- [29] V. Soltwisch, A. Haase, J. Wernecke, J. Probst, M. Schoengen, S. Burger, M. Krumrey and F. Scholze: 'Correlated diffuse x-ray scattering from periodically nanostructured surfaces'. In: *Physical Review B* **94.3** (2016), p. 035419. DOI: 10.1103/PhysRevB.94.035419.
- [30] J. Verhoeven, L. Chunguang, E. J. Puik, M. J. van der Wiel and T. P. Huijgen: 'Ion beam modification of Mo/Si multilayer systems for X-ray reflection'. In: *Applied Surface Science* **55.2** (1992), pp. 97–103. DOI: 10.1016/0169-4332(92)90099-J.
- [31] S. N. Yakunin, I. A. Makhotkin, K. V. Nikolaev, R. W. E. v. d. Kruijs, M. A. Chuev and F. Bijkerk: 'Combined EUV reflectance and X-ray reflectivity data analysis of periodic multilayer structures'. In: *Opt. Express* **22.17** (2014), pp. 20076–20086. DOI: 10.1364/OE.22.020076.



# Danksagung

Danke!



# Eidesstattliche Versicherung

Hiermit versichere ich an Eides statt, dass ich die vorliegende Arbeit selbstständig verfasst und keine anderen als die in der Dissertation angegebenen Quellen und Hilfsmittel benutzt habe. Alle Ausführungen, die anderen veröffentlichten oder nicht veröffentlichten Schriften wörtlich oder sinngemäß entnommen wurden, habe ich kenntlich gemacht. Die Darstellung des Eigenanteils an bereits publizierten Inhalten in meiner beigefügten Erklärung ist zutreffend.

Es gab keine Zusammenarbeit mit anderen wissenschaftlichen Mitarbeitern, die ein Promotionsverfahren anstreben.

Berlin, den 31. März 2017

Anton Haase



# Erklärung

Es wurden bereits Teile der Dissertation veröffentlicht.

Liste der Veröffentlichungen, welche in die Dissertation eingeflossen sind:

- 1) A. Haase, V. Soltwisch, C. Laubis und F. Scholze: „Role of dynamic effects in the characterization of multilayers by means of power spectral density“. In: *Appl. Opt.* **53.14** (2014), S. 3019–3027. DOI: 10.1364/AO.53.003019
- 2) A. Haase, V. Soltwisch, F. Scholze und S. Braun: „Characterization of Mo/Si mirror interface roughness for different Mo layer thickness using resonant diffuse EUV scattering“. In: *Proc. SPIE*. Bd. 9628. 2015, S. 962804–962804–7. DOI: 10.1117/12.2191265
- 3) A. Haase, S. Bajt, P. Hönicke, V. Soltwisch und F. Scholze: „Multiparameter characterization of subnanometre Cr/Sc multilayers based on complementary measurements“. en. In: *Journal of Applied Crystallography* **49.6** (Dez. 2016), S. 2161–2171. DOI: 10.1107/S1600576716015776
- 4) A. Haase, V. Soltwisch, S. Braun, C. Laubis und F. Scholze: „Interface Morphology of Mo/Si Multilayer Systems with Varying Mo Layer Thickness Studied by EUV Diffuse Scattering“. In: *Optics Express* (2017)

Liste der Veröffentlichungen, welche nicht in die Dissertation eingeflossen sind:

- 1) M. Prasciolu, A. Haase, F. Scholze, H. N. Chapman und S. Bajt: „Extended asymmetric-cut multilayer X-ray gratings“. EN. In: *Optics Express* **23.12** (Juni 2015), S. 15195–15204. DOI: 10.1364/OE.23.015195
- 2) V. Soltwisch, A. Haase, J. Wernecke, J. Probst, M. Schoengen, S. Burger, M. Krumrey und F. Scholze: „Correlated diffuse x-ray scattering from periodically nanostructured surfaces“. In: *Physical Review B* **94.3** (Juli 2016), S. 035419. DOI: 10.1103/PhysRevB.94.035419

Ich habe an keiner anderen Hochschule oder Fakultät eine Promotionsabsicht eingereicht.

Berlin, den 31. März 2017

Anton Haase

